GROWTH AND PROCESSING OF GALLIUM NITRIDE AT HIGH
TEMPERATURES IN AN ULTRA HIGH-PRESSURE REACTOR FURNACE

By

FRANCIS PATRICK KELLY

This work is dedicated in loving memory of my father, Dr. Edward J. Kelly, M.D. for his infinite patience, generosity, humor, love, and guidance.

ACKNOWLEDGMENTS

First and foremost, I would like to thank my advisor, Dr. Rajiv K. Singh for his support and guidance throughout my graduate career at the University of Florida. I would also like to thank all of the members of my supervisory committee, Dr. Stephen Pearton, Dr. Reza Abbaschian, Dr. Cammy Abernathy, and Dr. Fan Ren for all of their expertise and advice. I would like to thank Dr. Rolf Hummel who was my interim advisor my first semester at the University of Florida.

I would be remiss if I didn't extend my sincerest thanks to all of the people who advised and helped with the work that went into making this thesis. Thanks go to Dr. Don Gilbert, Dr. Robert Chodelka, Dr. Alexander Novikov, Dr. Nikolai Patrin and Dr. Henry Zhou for all of their work on the high pressure system and innumerable other things without which this work would not have been possible. Thanks also go to all of the people who helped with characterization, including Dr. Mark Eddy Overberg, Dr. Valentin Craciun, Dr. John Budai, Dr. Kevin Powers, Mr. Michael Ollinger, Mr. Joshua Howard, Mr. Nabil Bassim, Chad Essary, Mr. Jamie Rhodes, Mr. Gary Schieffle, Mr. Eric Lambers, Dr. Uday Mahajan, and Mr. Gil Brubaker.

Thanks go to Dr. Michael Stavola of Lehigh University for first kindling in me the scientific curiosity and interest in solid-state physics that I have today; and to Dr. Michael Evans for being a kindred spirit and continual source of humor, joy, and practical advice about life that has aided me immeasurably in my journey. And, last but not least, I want

TABLE OF CONTENTS

Abstract of Dissertation Presented to the Graduate School
of the University of Florida in Partial Fulfillment of the
Requirements for the Degree of Doctor of Philosophy

GROWTH AND PROCESSING OF GALLIUM NITRIDE AT HIGH
TEMPERATURES IN AN ULTRA HIGH-PRESSURE REACTOR FURNACE

By

Francis Patrick Kelly

May 2003

Chair: Rajiv K. Singh
Department: Materials Science and Engineering

We developed novel high-pressure techniques for the producing and processing

gallium nitride (GaN) at elevated temperatures using a specially designed high-pressure

reactor furnace. By working at high ambient pressures, we can suppress the tendency of

GaN to chemically dissociate at elevated temperatures. Thus we can affect the growth of

small crystals and promulgate microstructural changes in films grown on sapphire

substrates via other techniques.

GaN crystals were grown and films annealed in the high pressure furnace and results

investigated using a wide variety of qualitative and quantitative analytical

characterization techniques including scanning electron microscopy (SEM), x-ray

diffraction (XRD), micro-Raman spectroscopy, atomic force microscopy (AFM), optical

profilometry, Auger electron spectroscopy (AES), cathodoluminescence (CL) and

photoluminescence spectroscopy (PL), and energy dispersive x-ray spectroscopy (EDS).

CHAPTER 1
LITERATURE REVIEW

Background

Gallium nitride (GaN) is an important material in the semiconductor industry, because of its unique set of useful electronic and optoelectronic properties. Gallium nitride has a broad range of niche semiconductor applications, and much work has been done in the past ten years to improve the overall quality of GaN films for devices. Studies included investigations involving different heteroepitaxial substrates [1,2]; epitaxial lateral overgrowth (ELO) [3–5]; novel techniques for growing bulk GaN [6–14]; and growth of freestanding GaN wafers by vapor phase epitaxy (VPE) and subsequent separation [15,16].

Gallium nitride in its hexagonal wurtzite phase is a direct bandgap semiconductor with a fairly wide bandgap energy of 3.4 eV (Figure 1-1) [1]. These two properties alone make GaN an attractive semiconductor specifically for fabricating solid-state light-emitting diodes (LEDs) and lasers operating in the blue range, (Figure 1-2) [1]. Gallium nitride is also well suited to high power/high temperature/high frequency electronics applications again, because of its wide bandgap, good thermal conductivity, high breakdown filed, high electron mobility, and high saturation drift velocity. Some relevant physical properties of the common materials used for high temperature/high power/high frequency device applications include include electronic bandgap energy (E_g), dielectric breakdown field strength (E_B), electron mobility (μ_e), maximum electron drift

1

velocity (v_s), thermal conductivity (χ), and dielectric constant (ϵ). The combined figure of merit (CFOM) is the total rating of all relevant physical properties shown for device applications and is defined as the product of the aforementioned properties fo rthe material sin question, divided by those values for silicon. The CFOM contains a factor of E_B^2 though and is therefore more highly dependant on E_B than on any of the other properties. Two of the most relevant physical properties (bandgap energy and breakdown field strength) are better in GaN than in the other materials. Not surprisingly, GaN also has the highest CFOM [17].

Common dopants used in GaN for electronic applications include Si, S, Se, Te, and O as donors and Mg, Ca, Be and C as acceptors. Currently, the maximum achievable doping concentration combined figure of merit is 5×10^{20} (cm^{-3}) for sSi in GaN; and roughly 5×10^{18} (cm^{-3}) for Mg in GaN (cm^{-3}) [17]. Another valuable feature of GaN, perhaps the most valuable, is that it lattice matches to AlGaN and other nitrides and can be used for a wide variety of heterostructure devices such as heterojunction field effect transistors (HFETs) and heterojunction bipolar transistors (HBTs).

Gallium nitride has its own unique set of limitations however. Paramount among these is that, like other III–V compounds, an overpressure of the group V element, in this case nitrogen, is needed to prevent chemical degradation of GaN at the high temperatures needed for processing of GaN films. In the specific case of GaN the required pressures are high enough to make the problem of film decomposition quite severe. Other technical problems with GaN include its high theoretically predicted melting point (2500ºC) [18]) and the prohibitively low solubility of N in liquid Ga at 1 atm, which is roughly 0.0025 at.% at ~1600ºC [10]. This makes GaN bulk growth via the Czochralski

method unworkable. Thermally induced degradation also prohibits thermal annealing of extended defects in ion-implanted GaN films, as the required temperature for such is ~1650ºC (using the ~2/3 of the melting temperature rule-of-thumb).

Gallium nitride will start to outgas nitrogen near 800ºC, although the exact temperature at which nitrogen loss becomes a problem depends largely on the annealing ambient and the quality of the film [19–42]. This means that the selective area doping of GaN via ion implantation for electronic applications must be done in such a way as to minimize lattice damage during the implant. Even then, the ever-present lattice damage cannot be annealed out entirely. In addition to that, p-type conduction of GaN doped with Mg is difficult to achieve because ion-beam-induced lattice damage leads to the creation of n-type material. The implant defects produced will then compensate out the p-type dopant. If a high enough dose is used during implantation, extended defects will form in the near-surface region of the film. In GaN these usually take the form of planar defects parallel to the basal plane of the GaN lattice. These defects, as mentioned above, require prohibitively high annealing temperatures for their removal.

The low solubility and high melting point problems are both deleterious because of the constraints they place on the growth of GaN in bulk volumes. In order to get a sufficient amount of N dissolved into a liquid Ga melt, extremely high temperatures must be used to increase the N-solubility of liquid Ga. At such temperatures, extremely high pressures of N are needed to affect the growth of stable GaN. Therefore, production of reasonably large GaN boules is impossible using bulk growth techniques currently employed for other III–V compounds such as Liquid Encapsulated Czochralski (LEC) growth and the Bridgman growth method which are both feasible for the bulk growth of

gallium arsenide (GaAs), for example. This, in turn, makes the production of GaN substrates impossible insofar as conventional sectioning of boules to make wafers is concerned. Homoepitaxy of GaN films onto fairly large (2" diameter), bulk-grown GaN substrates is therefore beyond the reach of the current state of the art. As no such substrates exist, heteroepitaxy must be employed if GaN films are to be grown on wafers of a size suitable for device processing. This technique, however, is not without drawbacks and leaves some substantial issues of its own to be considered with regard to the microstructure, crystalline quality, and ultimate overall efficacy of the GaN produced.

The two most commonly used materials for GaN heteroepitaxy substrates found in the literature are silicon carbide (SiC, 6H-SiC, 4H-SiC) and sapphire (α-Al$_2$O$_3$). Both of these exhibit lattice mismatches with GaN large enough to cause the formation of high concentrations of misfit dislocations in the grown films. For 6H-SiC, the mismatch is 3.5% and for α-Al$_2$O$_3$ it is 1.5%. The dislocations in as-grown material usually consist mainly of threading dislocations and stacking faults, but some authors also report dislocation loops [43]. Gallium nitride wafers that are currently available suffer from many of the same problems of heteroepitaxial GaN film growth. They generally have a high concentration of dislocations because they are grown heteroepitaxially on foreign substrates using gas-phase epitaxy techniques such as molecular beam epitaxy (MBE) and vapor phase epitaxy (VPE) [44] and are then separated from the substrate wafer.

Thermodynamics

Since it is the stability or decomposition of GaN at elevated temperatures that is the primary concern here, the thermodynamics of the reaction:

$$GaN = Ga + \tfrac{1}{2}N_2 \tag{1-1}$$

will be of great usefulness to have explored. The reaction will either proceed from right to left or from left to right, depending on Gibbs free energies of the separate reaction participants. The Gibbs free energy of one component is defined as:

$$G_x = H_x - TS_x \qquad (1\text{-}2)$$

where H_x is the enthalpy and S_x is the entropy of component "x". The direction the reaction will take, that is, the stability of either GaN or of Ga and N_2 gas under varying thermodynamic conditions, is dictated by the change in the total Gibbs free energy of the system in going from one side to the other.

$$\Delta Grxn = G_{GaN} - (G_{Ga} + \tfrac{1}{2}G_{N2}) \qquad (1\text{-}3)$$

When the system is in equilibrium, $\Delta Grxn = 0$, and the two sides of the reaction are balanced. If $\Delta Grxn < 0$, then the thermodynamic state of the system favors stability of GaN. Likewise, if $\Delta Grxn > 0$, then the Ga + N_2 side is the stable one. Figure 1-3, taken from Porowski et al. [6], shows a set of superimposed Gibbs free energies of the different components of the reaction described by equation (1-1) plotted versus temperature and assuming a constant pressure (of N_2 gas) of 1 bar (1.01 atm). The combined total Gibbs free energy of Ga + $\tfrac{1}{2}N_2$ (the right side of Equation 1-1) is also plotted. Note the point at ~830 °C where the GaN and Ga + $\tfrac{1}{2}N_2$ curves cross. This is the predicted temperature at which GaN becomes unstable, as it no longer has the lowest Gibbs free energy.

As the temperature of the system rises above this predicted threshold (assuming an ambient pressure of 1 bar of N_2 gas) there is an increase in the driving force toward decomposition of GaN into Ga and N_2 gas, since those components combined have a lower total Gibbs free energy at temperatures above the threshold, and are therefore stable. Figure 1-4, also taken from Porowski et al. [6] shows the effect of increased N_2

pressure on the Gibbs free energies of several III–V metal nitride systems. In the three cases shown (AlN, GaN, and InN), the Gibbs free energy of the metal nitride (MeN, where Me is Al, Ga, or In) side of the equation is, to a first approximation, constant as the volume of the solid does not change to any large extent under increased ambient pressure. That leaves the right hand side of the equation, namely the combined Me + ½N$_2$ which does exhibit a shift in Gibbs free energy under increased ambient pressure, as indicated by the dotted lines.

Note, there is only one dotted line drawn for Me + ½N$_2$. Separate Ga, In, and Al curves are not necessary, as the fact that they are in a condensed phase makes their overall Gibbs free energy shift negligibly small. The main contribution to this shift is from the N$_2$ gas. Being a compressible fluid, N$_2$ shows a large change on free energy as a function of pressure, which is not surprising as the volume change under pressure is much higher for gasses than for the relatively uncompressible condensed phases [6–9, 17, 18, 19]. Another important consideration in the thermodynamics of GaN research is the high activation energy (379 kJ/mol) for the decomposition of GaN [24] via the reaction:

$$2GaN = 2Ga + N_2 \tag{1-4}$$

Pisch et al. [23] found that GaN annealed in an Ar + 5%H$_2$ ambient was unperturbed after a 30-minute anneal at 800°C in contrast to GaN films annealed with Ga droplets placed on the surface. Those films showed degradation of the GaN in the region immediately surrounding the Ga droplets after anneals at 720°C, in a similar ambient. This shows that Ga droplet formation is the rate-limiting step for surface decomposition of GaN in such an ambient, as has been mentioned or alluded to in other works in the literature by

Porowski, Karpinski, and Van Vechten at different times throughout the development of GaN related research work [10, 18–21].

Bulk Growth

The main thrust of high-pressure GaN bulk growth research in the last five years has largely been conducted by, or in collaboration with, S. Porowski at the High Pressure Research Center at the Polish Academy of Sciences in Warsaw. In their growth chamber they are able to realize nitrogen overpressures of up to 20 kbar of nitrogen gas and can achieve temperatures up to 2000°C. Taking advantage of the increased nitrogen solubility of liquid gallium at elevated nitrogen pressures and elevated pressures (see Figures 1-5 through 1-7), they have produced hexagonal, freestanding, monolithic GaN platelets with lateral dimensions of up to 10 mm and thicknesses of about 0.2 mm [6,7]. However, smaller crystals that they have grown are of a higher quality than the largest 10 mm wide crystals, which represent the maximum size they have attained. Rocking curves taken from the smaller (2.5 mm x 2.5 mm lateral sized) crystals, grown under conditions commensurate with slower growth rates have shown a full width at half maximum (FWHM) of 23–32 arcsec whereas the larger 10mm crystals general have a FWHM of at least 40 arcsec and has high as 60 arcsec [7]. The smaller GaN crystals, grown at a slower overall growth rate, are monocrystalline whereas the larger exhibit a mosaic texture with low angle boundaries. They provide a theory as to why this occurs, involving the relief of stresses caused by migration of Ga toward the N-terminated side of the crystal [45]. They have also grown crystals with and without Mg present in the melt thereby producing both insulating and conducting bulk material. Crystals grown with Mg incorporation are the most insulating and have resistivities as high as 10^6 Ωcm, whereas crystals grown without any Mg in the melt show conducting behavior and have

resistivities in the range of 10^{-3}–10^{-2} Ωcm with electron concentrations of 3–5 x 10^{19} cm^{-3} due to N vacancies in the undoped GaN.

Theoretical calculations made by Van Vechten [18] indicate that the melting temperatures of nitrides are much higher than the maximum temperature available for each of the compounds in most commercially available crystal growth systems. Hence, there is a very low solubility of AlN, GaN, and InN in the corresponding liquid melts. Figures 1-6 and 1-7 show the temperature dependence of N concentration in liquid Ga metal for the Ga-GaN system. The solid line represents the calculated values assuming behavior of the solution and the melting point data for GaN proposed by Van Vechten [18] (melting point temperature of 2790 K and entropy change at melting of 16 kcal per mole). These data indicate that, for the case of Ga metal melts, the nitrogen concentration may be increased up to or perhaps even exceeding 1 at. %, which is sufficient for effective crystallization from solution. Figure 1-8 shows two graphs stacked vertically to illustrate the temperature, pressure, and nitrogen concentrations achievable in the author's experimental apparatus [10]. Note that if the pressure could be increased the nitrogen solubility could be increased beyond even their estimations.

Karpinski et al [19] did experiments to determine the stability of GaN in two different high pressure systems of interest. Their work led to a determination of the GaN-N phase diagram shown in Figure 1-9. The surprising part of their results is the backward-bending phase boundary shown as a solid line as compared to the straight, dotted line which one would predict deriving the phase boundary from the assumed thermodynamics of GaN and N_2 gas using the ideal gas law as the equation of state for N_2 gas. Karpinski and Porowski et al. show [19] that this deviation at high pressures can be

explained if one takes into account non-ideal behavior of diatomic nitrogen gas, using the virial equation as the new equation of state.

These data suggest that GaN is the one significant III-V nitride material that is most ideally suited for high-pressure crystal growth research. As can be seen in Figures 1-3, 1-4 and 1-5, aluminum nitride (AlN) requires much higher temperatures than are available in the cited author's system, as well as any other high pressure growth system known. For the case of InN, the limiting factor is the high pressure needed. In the author's system, 20kbar is the upper limit. While the high pressure system used for this work has a somewhat higher upper pressure limit, InN is still significantly less attractive than GaN for this reason.

In recent years, several groups have attempted to produce freestanding large-area GaN substrates by vapor phase epitaxy (VPE) of GaN onto foreign substrates and subsequent separation of the thick GaN layer from the VPE substrate. O. Kryliouk et al. [15] at the University of Florida have produced 10 x 10 x 0.3 mm free standing GaN crystals by growing GaN via hydride MOVPE onto lithium gallium oxide ($LiGaO_2$) substrates which are well lattice-matched to the GaN lattice (~1% lattice mismatch). The $LiGaO_2$ material was grown using the Czochralski method. These GaN films spontaneously separated from the substrates upon controlled cooling after the growth, due to surface preparation. R.J. Molnar et al. [46] have investigated different surface pretreatments in an attempt to obtain freestanding GaN substrates. The main barrier in their efforts to produce large-area, freestanding GaN crystals lies in the separation of the GaN films from their sapphire substrates. The method of first growing a ZnO buffer

layer onto the sapphire and etching it away after GaN growth is limited due to thermal cracking of the ZnO layer during cooling.

By far the most overall success in producing freestanding GaN wafers via VPE growth and subsequent separation has been reported by M. Kelly et al. [16] at Advanced Technology Materials Inc. They report the production of a freestanding GaN wafer nearly as large as the 2" diameter substrate that it was grown on. A high-temperature laser processing technique was used to separate the thick (250–300 µm) GaN film grown from its sapphire substrate. They used a neodymium: yttrium-aluminum-garnet (Nd:YAG) pulsed laser operating at 355 nm (commensurate with a photon energy of ~3.49 eV, just slightly larger than the GaN bandgap) to thermally decompose a thin layer of GaN at the GaN/sapphire interface. Minimal bowing of the wafer occurred, as they performed the laser processing at temperatures of over 600ºC.

Annealing

There has been a continuous stream of effort published in the literature based on annealing of GaN films, more, by far, than that based on bulk growth, as GaN films are quite readily grown on foreign substrates. Recent work in the last ten years [21–44] has produced a wealth of data on the behavior of GaN heteroepitaxial films. Several different substrates have been used, including sapphire and SiC. A large variety of different dopants has been reported on, including silicon (Si), magnesium (Mg), and calcium (Ca) to name a few, as well as rare earth lanthanide elements like europium (Eu) and erbium (Er) [47–52].

Annealing of GaN films doped for electronic applications is necessary to remove lattice defects caused by the collisional nature of the ion implantation process as well as to promote the implanted species into substitutional lattice sites and activate them

electrically. Since electronic devices require selected area doping via ion implantation, a good understanding of the behavior of GaN films under annealing conditions is critical. As mentioned earlier, GaN has a tendency to decompose into gallium metal and nitrogen gas at elevated temperatures in excess of 800°C [17]. This makes thermal annealing of GaN at high enough temperatures to affect full removal of ion beam-induced lattice disorder difficult. As such, a great deal of effort is underway in this area to find a method of removing post-implant disorder without chemical degradation of the film due to nitrogen loss at the surface.

Two of the most successful techniques employed thus far are 1) capping the GaN film with reactively sputtered aluminum nitride (AlN) to inhibit nitrogen loss at the GaN surface, and 2) placing a second GaN film wafer on top of the first such that any nitrogen loss out of one wafer will act as a source of nitrogen overpressure on the second, since the two wafers are in such close proximity to each other. In almost all instances, rapid thermal annealing (RTA) is employed to reduce the amount of time the wafers spend at elevated temperature. This is an important factor in minimizing dopant redistribution in the film. Furthermore, decreasing the heating time minimizes the amount of nitrogen that can outgas from the surface and hence prevents gallium droplets from nucleating on the surface.

H. H. Tan et al. [26] report on using the proximity method to anneal GaN films implanted with Si and Te at various doses, in order to investigate the damage removal in GaN as a function of implant dose, implant temperature, and annealing temperature. They used an RTA annealing system and annealed at or below 1100°C. They found that even RTA at 1100°C was insufficient to completely remove implant damage in GaN

films that were ion implanted at temperatures up to 200ºC. In their study, even those films implanted with Si at doses below 10^{14}cm^{-2} show residual damage. They also found, not surprisingly, that heavily disordered (but still pre-amorphous) GaN films were not restored upon annealing at 1100ºC, and furthermore, that amorphized films annealed the same way recrystallize into a polycrystalline structure.

R.G. Wilson et al, using the AlN cap method [25] performed experiments involving rapid thermal annealing of GaN wafers ion-implanted with sulfur (S), tellurium (Te), silicon (Si), beryllium (Be), and carbon (C) at temperatures up to 1450ºC. They report that no appreciable dopant redistribution was observed in any of their annealing experiments except those that were doped with Be, which, they've deduced, exhibits broadening of the SIMS profile due to defect-assisted diffusion in GaN at 900ºC. They report that the annealing of AlN-capped, Si$^+$-implanted GaN at 1400ºC was much more effective in removing post-anneal damage than more conventional anneals at 1100ºC.

Porowski et al. [12] have also investigated annealing of gallium nitride doped with magnesium (GaN:Mg). This work included both bulk that they grew, and homoepitaxial and heteroepitaxial GaN films doped with Mg) in their high-pressure system. They annealed GaN:Mg at temperatures ranging from 1200ºC to 1500ºC under N$_2$ pressures of 10–15 kbar. They report that their method of annealing GaN:Mg films (both heteroepitaxial and homoepitaxial films grown on GaN:Mg bulk they grew in the same chamber) produced semi-insulating material with the characteristic blue luminescence at roughly 3 eV. They also found that heteroepitaxial films show the highest diffusivity of Mg into the GaN films. They conclude this shows that dislocations are the main paths of Mg diffusion into GaN, as the heteroepitaxial films are characterized as having a

dislocation density of 10^{10} cm^{-2} whereas, in the homoepitaxial films, the dislocation density is only 10^5cm^{-2}.

Device Development

The more attractive electronic and optoelectronic properties of GaN have been well known for over thirty years now and so it is no surprise that research efforts have proceeded in the area of GaN-based device fabrication for that time period. The first example of a heteroepitaxially grown GaN film was published by Maruska and Tietjen in 1969 [53–55]. They were the first to achieve GaN film growth using vapor phase epitaxy and improvements have been continually made in GaN film growth technology for LEDs and other optoelectronic devices ever since. For example, in 1971, the first GaN metal-insulator-semiconductor (MIS) LED was fabricated by Pankove et al. [56], and in that same year, the first GaN film ever grown using MOCVD was demonstrated by Manasevit et al [57]. Three years later, Akasaki and Hayashi [58] became the first to publish work demonstrating GaN film growth by molecular-beam epitaxy (MBE).

In 1986, Amano et al [59] reported the first ever growth of ~3.5–4.5 micron thick GaN films with optically flat surfaces by growing GaN films via metal-organic vapor phase epitaxy (MOVPE) on sapphire (0001) substrates. They accomplished this by first growing a thin, amorphous buffer layer of AlN on the substrate and subsequently growing the GaN film layer on top of that. The various measured morphological, optical, and crystalline properties of the GaN films they grew with this method were all either better than or comparable to other films in the literature by this processing step, and they obtained an x-ray rocking curve (XRC) with a FWHM of 2.7 min from the GaN (0006) reflection, which was by far the best such data ever reported at the time it was published.

The authors reported that the overall crystalline, optical, and microstructural quality of the GaN films grown in their study was primarily a function of three important growth parameters. The first two of those parameters were the thickness and deposition temperature of the AlN buffer layer, and the third was the growth temperature of the GaN layer. They found that the GaN films exhibited polycrystalline microstructure if the AlN buffer layer deposition time exceeded one minute, whereas the GaN films grown on top of AlN buffer layers that were deposited at temperatures below 800°C exhibited significant pitting and those grown atop buffer layers deposited at over 1100°C showed hexagonal polycrystalline grains microstructures. The GaN films grown at less than ~950°C showed pitting, whereas the films grown at temperatures exceeding ~1050°C exhibited significant film cracking. The authors also reported that their photoluminescence (PL) data suggest a fairly low density of deep level impurities, and they reported a lower intensity of the yellow emission of GaN than any authors previously had achieved. Three years later the same authors reported the first production of p-type GaN doped with Mg and demonstrated the first GaN-based junction LED.

In 1992, Khan et al. [60] reported the presence of a two-dimensional (2-D) electron gas in a GaN-AlGaN heterostructure which they grew using low pressure MOCVD. This work was also the first ever example of a 2-D electron gas in a wide-bandgap, hexagonal wurtzite system, and formed the basis for high electron mobility transistor devices in the $Al_xGa_{1-x}N$ ternary alloy material system. The authors based their conclusions (specifically the presence of a 2-D electron gas) upon their observation of step-like features in the measured magnetoresistance curves obtained by performing quantum Hall effect experiments on the AlGaN-GaN heterostructures that they grew.

They reported the 2-D mobility for their heterojunction device to be 834 cm^2/Vs at room temperature and that the mobility monotonically increased to a saturation value of 2626 cm^2/Vs as temperature was decreased to the 77 K liquid nitrogen boiling point, and remained nearly constant down to the 4.2 K liquid helium temperature. They found that the peak mobility increased with increasing aluminum concentration on the AlGaN layer up to a maximum concentration of 13 at. %, at which point the 2-D mobility began to monotonically decrease in a manner very similar to the behavior of 2-D GaAs-AlGaAs heterojunction device structures [61]. They attributed this decrease with increasing Al concentration to several factors including lattice strain due to increased lattice mismatch with the GaN layer as the Al concentration in the Al layer is increased. They estimated their 2-D carrier concentration to be on the order of 10^{11} cm^{-2} using the Shubnikov-Haas (Sd-H) method.

The GaN-AlGaN system has a bandgap that is tunable from 3.4 to 6.2 eV which, among other desirable properties, makes it highly suited for the fabrication of high-performance devices requiring high operating temperatures. So it is very noteworthy that a year later, in 1992, Khan et al. [62] then demonstrated the first GaN-based metal-semiconductor field effect transistor (MESFET) ever produced in the laboratory. They used low pressure MOVPE to grow a 600nm thick unintentionally doped n-type GaN layer on top of a sapphire substrate using the AlN buffer layer method of their previous work, and then used standard photolithographic techniques to pattern 100X200 μm metal mesas on top of the GaN layer. The GaN layer formed the conducting channel for the device and the source and drain ohmic contacts were made of titanium aluminum (TiAl), while the rectifying (Schottky) contact was made of silver (Ag). The devices which they

fabricated in this way had a gate length of 4μm, a gate width of 100μm, and a channel opening of 10μm. This device exhibited a transconductance of 23 mS/mm at a gate bias of -1V, and they observed complete pinch-off of the current at a gate potential of -12V.

Just one year later, the same group, Khan et al. [63], also produced the first GaN-AlGaN-based high electron mobility transistor (HEMT), based on their earlier work. They grew a 100nm thick layer of $Al_{0.14}Ga_{0.86}N$ on top of a 600nm thick GaN layer grown on buffered sapphire using very similar device geometry and dimensions to their previous MESFET device, and they fabricated a heterojunction that created a 2-D electron gas at the GaN-AlGaN interface, which they show dominated the electrical properties of the channel in the HEMT device they fabricated. The HEMT they obtained had a transconductance of 28 mS/mm at 300K and 46 mS/mm at 77K. Both were obtained at a gate bias of +0.5V, and complete pinch-off was observed at a -6V gate bias.

The next year, 1994, saw the demonstration of the first candela-class blue LED by Nakamura et al. in Japan [64]. They achieved then-unheard-of electroluminescence intensities in the blue by fabricating a double-heterostructure (DH) LED device out of GaN, AlGaN, and InGaN which used a Zn-doped InGaN layer as the active layer in the structure. The device realized a typical output power of 1500μW and an external quantum efficiency of as high as 2.7% at a forward current of 20mA at room temperature. This DH LED had a luminous intensity of more than 1 cd, which at the time was a real breakthrough in state-of-the-art blue LED technology. They recorded electroluminescence spectra from the device which showed an increase in intensity with increasing current up to 40mA with the peak centered at 450nm and with a FWHM of 70nm.

This work began what would become a long and fruitful line of research in GaN-based blue and green LEDs and semiconducting laser diodes for years to come, and allowed for the possibility of developing better flat panel displays in the future since technology of the time required two blue LEDs for every pixel to achieve enough blue brightness for the display to function within desired operational parameters. What's more, this work served as a jumping-off point for Nakamura et al and led to their eventual production of the first blue laser diode two years later,

1994 also saw the first measurements of GaN devices for high-power microwave frequency FET devices. Binari et al. [65] were the first group to produce a GaN-based microwave MESFET. They grew unintentionally-doped GaN on buffered sapphire (0001) substrates via MOVPE and proceeded to fabricate their MESFET. The ohmic contacts were a similar Ti/Al to previously mentioned work, but the metal they chose for the gate contact was gold (Au) and not the silver that other authors mentioned had used. Their device geometry had a gate length of 0.7μm and a source-to-drain spacing of 5μm. The measured transconductance of their devices was 20mS/mm and the high frequency characteristics they measured were comparable to existing silicon carbide (SiC) MESFET devices at the time (f_T and f_{MAX} of 8 and 17 GHz respectively).

This work was crucial in identifying some of the technological hurdles that high frequency GaN device research would need to get over in order to make commercially useful GaN-based microwave devices a viable market entity. First, the ohmic contacts had high contact resistances and the authors pointed out that higher carrier concentrations and improved contact technology would be needed, and second the need for enhanced frequency performance would require a shorter gate length and modification of the

channel doping. Experimental work on metalization schemes for ohmic contacts for GaN-based devices continues to this day and the thermal annealing which is often required to insure intimate physical contact between that metal and the nitride layer is a key issue in that arena.

Khan et al. [66] also produced the first GaN-based microwave frequency heterojunction field effect transistor (HFET) in 1994 at APA Optics Inc. in Minnesota. They fabricated a device with a gate length of 250nm and a source-to-drain separation of 2μm using an $Al_{0.13}Ga_{0.87}N/GaN$ heterojunction structure which consisted of a 250nm thick $Al_{0.13}Ga_{0.87}N$ layer grown on top of a 600nm thick GaN layer with an unintentional n-type doping of $1x10^{17}$ cm^{-3}. Their device exhibited a maximum extrinsic transconductance of 26mS/mm at room temperature, which they show was limited by the series resistance of the source. The device also exhibited an excellent pinch-off characteristic and low parasitic output conductance in saturation. They measured a cutoff frequency (f_T) of 11 GHz and a maximum oscillation frequency of 35 (f_{MAX}) GHz which were at the time superior to any other such measurements reported in the literature for the other leading HFET material system, which was SiC.

Pankove et al. [67] produced the first high-temperature heterojunction bipolar transistor (HBT) device incorporating GaN in 1994. They grew their device structure using liquid phase epitaxy (LPE) to grow the SiC layer on top of the SiC substrate, and then subsequently grew the GaN emitter layer on top of that using MBE after first cleaning the surface with hydrofluoric acid (HF) and degassing it at 1000 C under ultra-high vacuum (10^{-10} Torr). They measured a current gain as high as $1x10^5$ which exhibited near-ideal current-voltage characteristics with the exception of a leakage

current at voltages in excess of 10V. They reported high temperature operation up to 260 C with minimal degradation in output, but an increase in leakage current.

Ozgur et al. [68] produced the first GaN-based modulation doped field effect transistor (MODFET) in 1995. This work is very notable because their measured transconductance value was almost an order of magnitude greater than any previous work reported using any device geometry or growth scheme. They fabricated a normally-off (enhancement mode) device with a gate length of 3μm and a channel length of 5μm which exhibited an extrinsic transconductance of 120mS/mm and passed current of 300mA/mm with a 3V gate bias. Their device had a measured carrier mobility of greater than 1000 cm^2/Vs at 40K which dropped to ~490 cm^2/Vs at 310K. The device also exhibited a sheet carrier concentration of ~10^{13} cm^{-2} which was then about an order of magnitude greater than any previously reported data for the leading devices of the time, which were composed of GaAs/AlGaAs and/or InGaAs/InAlAs. This carrier concentration was, for all practical purposes, essentially independent of temperature, as it went from ~$1x10^{13}$ cm^{-2} to only $1.2x10^{13}$ cm^{-2} over the temperature range from 40K to 200K.

Another noteworthy development in 1995 was the first ever determination of the electron effective mass in GaN reported by Drechsler et al [69] in Munich. They recorded a cyclotron resonance transmission spectrum of a 3μm thick unintentionally doped GaN film on buffered AlN via MOVPE. The experiment was performed with a CO_2 far infrared (FIR) laser and the sample was cooled to 6K in a cryogenic cooled bolometer, which served as a detector. The magnetic field used varied from 0T to 9T and was oriented parallel with the c-axis of the GaN wurtzite structure. They were able to

obtain a direct measurement of the band-edge electron effective mass of $0.20 \pm 0.005 \, m_o$

for the GaN sample they grew from an experimental fit to the data using the equation:

$$P \, \alpha \, (1 + \omega_0^2\tau^2 + \omega_c^2\tau^2 \,)Ne^2\tau \, \Box \, [(1 + \omega_c^2\tau^2 - \omega_0^2\tau^2)^2 + 4\omega_0^2\tau^2]m^* \qquad (1\text{-}5)$$

and assuming a polaron coupling constant (α) of 0.49 of Barker et al. [70].

Sakai et al. [71] in Japan were the first to fabricate a high-quality GaN/GaInN

double heterostructure light emitting diode (DH LED) in 1995. They used MOVPE and

MBE to grow their device structure. The device showed intense near-edge

photoluminescence (PL) and exhibited intense violet emission upon current injection at

room temperature as seen in the electroluminescence spectra. This work was key in

establishing that GaN, upon further device optimization, could be used to fabricate short-

wavelength light sources such as LEDs via MBE with efficiencies higher than those

incorporating only MOVPE-grown GaN, and led to the realization of a MBE-grown

GaN-based laser diode within the near future.

In 1996 Khan et al. [72] improved upon their earlier work on GaN-based

microwave frequency HEMT devices by making the first such device with an

intentionally-doped channel. They reported a cutoff frequency of $f_T = 36.1 \, GHz$ for a

short-channel device ($0.25 \mu m$), which was the highest for any such device made form

any wide-bandgap material at the time. They reported that their simulations based on

earlier work predicted that the device performance would be better if the carrier

concentrations could be improved, and this was borne out by the results in this later

study.

The first work on a GaN-based junction field effect transistor (JFET) device

fabricated with ion implantation doping as a processing step was published by Zolper et

al. [73] in 1996. The device was fabricated out of GaN grown on sapphire and subjected to 8 important processing steps. First, the n-type channel was ion implanted with ^{28}Si and the p-gate region was implanted with ^{40}Ca. Second, the 300nm thick tungsten (W) gate contact was sputter deposited on top of the p-gate. Third, the gate contact was patterned by reactive ion etching (RIE) using an SF_6/Ar plasma. Fourth, the source and drain regions were selective-area, non-self aligned ion implanted with ^{28}Si and, following that, the fifth step was a rapid thermal anneal (RTA) procedure at 1150 C for 15s to activate all the implanted dopants. Sixth, the p-GaN layer was etched to separate it from the n-GaN source and drain regions by electron-cyclotron resonance (ECR) plasma etching using a BCl_3/H_2/Ar plasma chemistry. Seventh, the Ti/Al source and drain contacts were patterned, and eighth, the source and drain contacts were alloyed by a second (alloying) anneal at 500 C at 15s.

The JFET device thus fabricated, the first ever of its kind made with GaN, was the characterized and exhibited a gate turn-on voltage of 1.84 V at 1mA/mm of gate current. The authors also reported that, for a ~1.7µm X 50µm JFET with a -6V threshold voltage, they achieved a maximum transconductance of 7mS/mm at V_{GS} = -2V and a saturation current of 33mA/mm at V_{GS} = 0 V. They further report that, with improved source and drain implant optimization, the performance should be improved markedly. This was excellent news for the production of GaN-based high-temperature/high-power devices, as the JFET device structure, which had not been previously demonstrated in GaN, is more ideally suited to such applications due to the inherently high gate turn-on voltages and low leakage currents the JFET device structure has as compared to, say, the MESFET or

HFET device geometries. Also, the fact that the channel in the JFET device is effectively buried, makes it more inherently robust.

Also in 1996, Wu et al. [74] reported that two different MODFET devices which they fabricated, one with only unintentional doping and a second that was doped with Si. The two devices they reported on had gate-to-drain breakdown voltages of up to 340 V for the unintentionally doped device and 240 V for the device that was doped with Si. These breakdown voltages were by far the highest ever reported at the time. The devices exhibited extrinsic transconductances of 100 to 140 mS/mm, and full channel currents of 150 to 400 mA/mm. But by far the most exciting development in GaN in 1996 was Nakamura's fabrication of the first blue laser diode, the complete details of which can be found in the his book "The Blue Laser Diode: The Complete Story" [75] which makes for interesting reading not only to the cogniscenti of the semiconductor device industry, but also to the casual reader with an interest in technological breakthroughs in general.

Work on GaN-based devices continued throughout the late 1990s and into the new millennium and device structures that had been previously demonstrated were improved significantly as time went on. In the high-power arena, for example, work continued by Wu et al. [76], Thibeault et al. [77], and, in 1998, Sullivan et al. [78] reported on an AlGaN HFET device grown on SiC which exhibited a total power of 2.3W at 10GHz. McCarthy et al. [79] reported on the fabrication of the first AlGaN/GaN HBT in 1998 as well, and Mishra et al. reported on the first HEMT grown using lateral epitaxial overgrowth (LEO). Schmitz et al. [54] reported on the complete menagerie of metal contacts to n-type GaN in 1998 as well and reported that the I-V characteristics scandium (Sc), halfnium (Hf), zirconium (Zr), aluminum (Al) and vanadium (V) were

nearly linear while those of niobium (Nb), titanium (Ti), cromium (Cr), and tungsten (W) were slightly rectifying. The metals in their study that exhibited strongly rectifying behavior were silver (Ag), gold (Au), copper (Cu), cobalt (Co), palladium (Pd), nickel (Ni) and platinum (Pt). In their work they determined that the Schottky barrier heights for the metals on GaN increased with increasing work function of the metal, but not follow a unity slope linear dependence, which is predicted by the Schottky theory. They found that GaN had a density of surface states similar to CdS, which is almost an order of magnitude less than that of GaAs.

Ren et al. [80] fabricated the first GaN metal oxide semiconductor field effect transistor (MOSFET) in 1998 as well. They reported that the device which they made, which was a $Ga_2O(Gd_2O_3)$/GaN depletion mode (normally off) MOSFET, exhibited significantly less leakage current at elevated temperature than conventional MESFET devices made on the same GaN layer. The MOSFET I-V characteristics actually improved upon heating to 400 C, which, upon modeling the effect of temperature on contact resistance, led the authors to conclude that the improvement was due to a reduction in the parasitic resistances present in the device.

The work on GaN, begun in 1969, has continued as a subject of great interest for the last thirty years and shows no sign of stopping any time soon. Selected physical data for GaN, collected from various sources over that time period and into the present day, are tabulated from various sources [53, 69, 80–84] and presented in Table 1-1.

Table 1-1. Selected physical data for GaN

Crystal Structure	Wurtzite	Lattice constant, a (Å)	3.189
Denisty (g/cm^3)	6.15	Lattice constant, c (Å)	5.185
Static dielectric constant	8.9	Electron mobility (cm^2/Vs)	1000
High frequency Dielectric constant	5.35	Hole mobility (cm^2/Vs)	30
Bandgap energy (eV)	3.39	Hole lifetime (ns)	~7
Electron effective mass (m$_e$)	0.20	Hole diffusion length (m) (at 300K)	~0.8x10^{-6}
Thermal conductivity (W/cmK)	1.5	Breakdown field (V/cm)	>5x10^6

This work has been of immeasurable importance to a number of concerned parties, including the consumer electronics industry, the energy industry, the military, and the scientific community as a whole. Gallium nitride-based electronic and optoelectronic semiconductor devices of nearly all conceivable kinds have been demonstrated, using various different techniques. From the early work of pioneers like Akasaki, Nakamura, and Van Vechten to the continued efforts of more recent authors, the combined effort of mankind's search knowledge about GaN has been both copious and fruitful. On can but hope it will continue to be so for years to come.
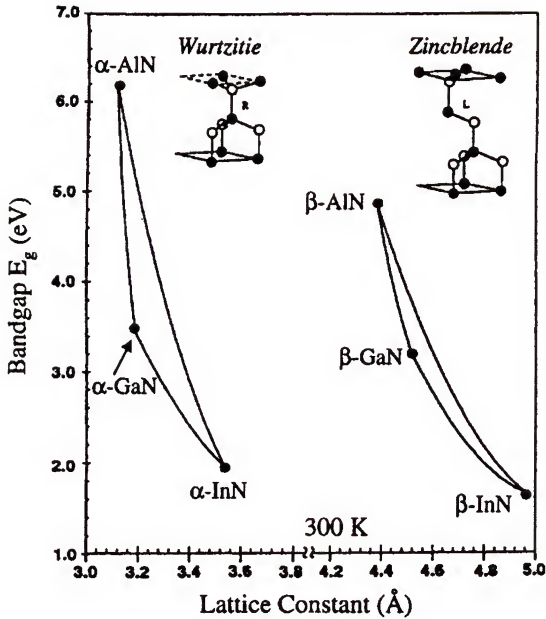
Figure 1-1. Bandgaps of selected hexagonal (alpha) and cubic (beta) phase III-Nitrides and their alloys plotted versus lattice constant a_0
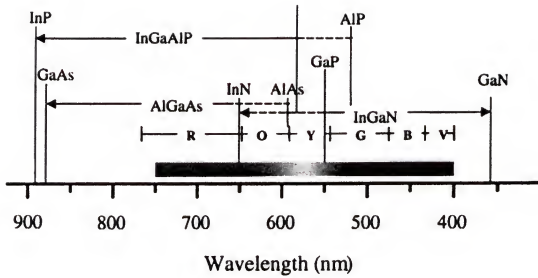
Figure 1-2. Wavelength ranges for possible LED devices made from various compound semiconductor materials
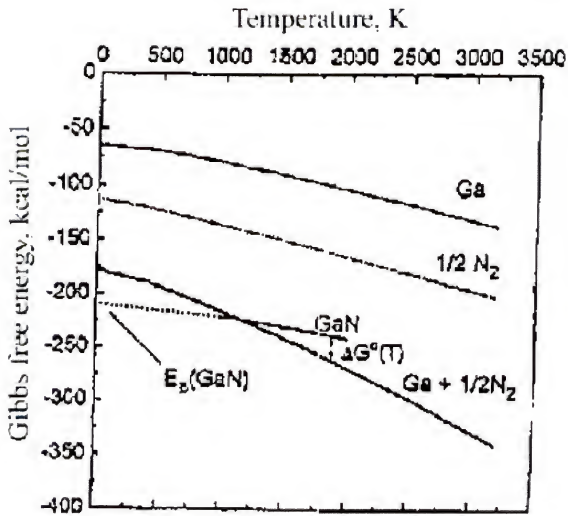
Figure 1-3. Gibbs free energies of interest in the GaN system
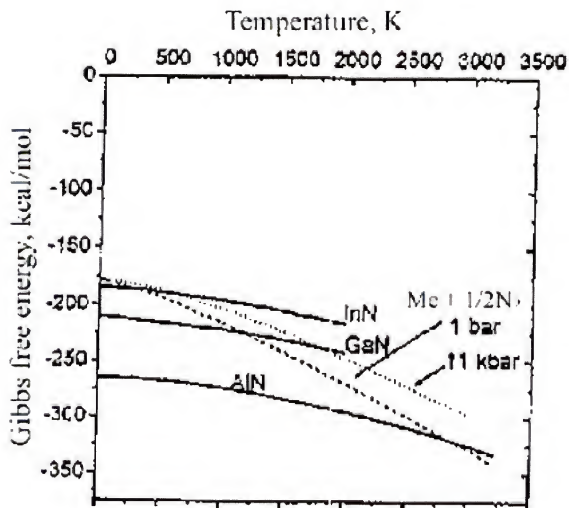
Figure 1-4. Pressure-induced shift in Gibbs free energy of Me + ½N₂
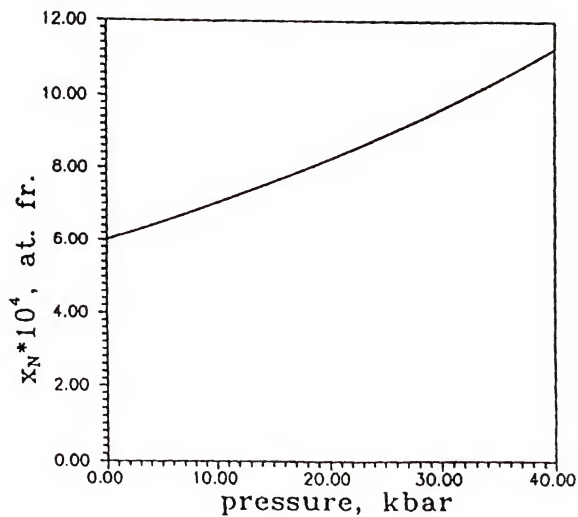
Figure 1-5. Maximum equilibrium concentration of nitrogen in liquid gallium versus pressure.
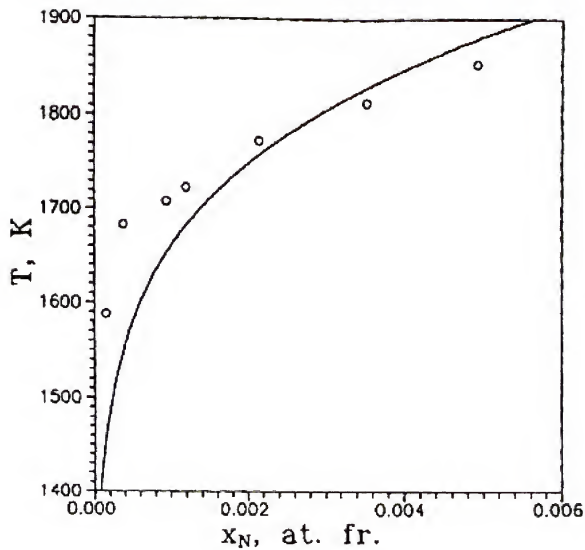
Figure 1-6. Data superimposed on predicted liquidus line for the Ga-GaN system
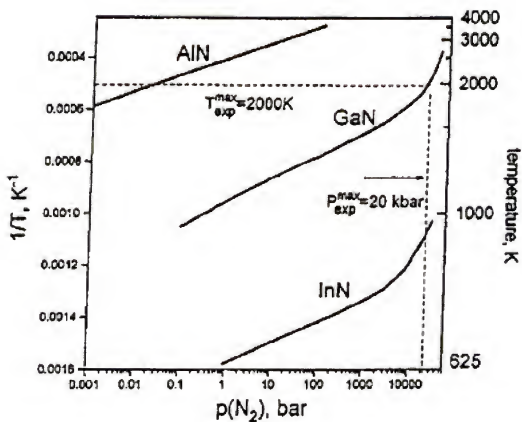
Figure 1-7. Equilibrium nitrogen gas pressure over selected III-V nitrides.
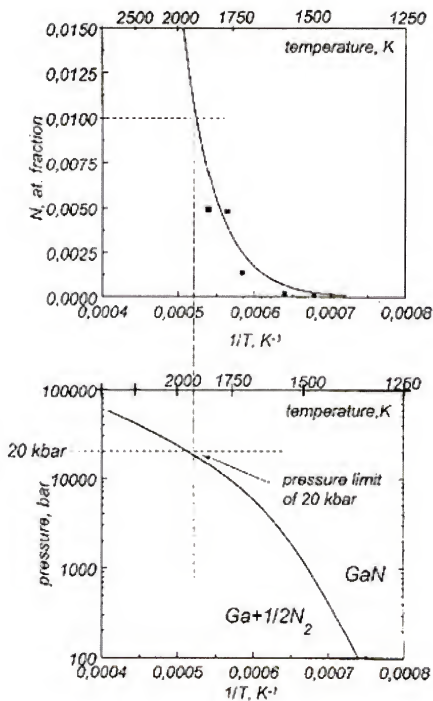
Figure 1-8. Atomic fraction of nitrogen and pressure versus inverse temperature.
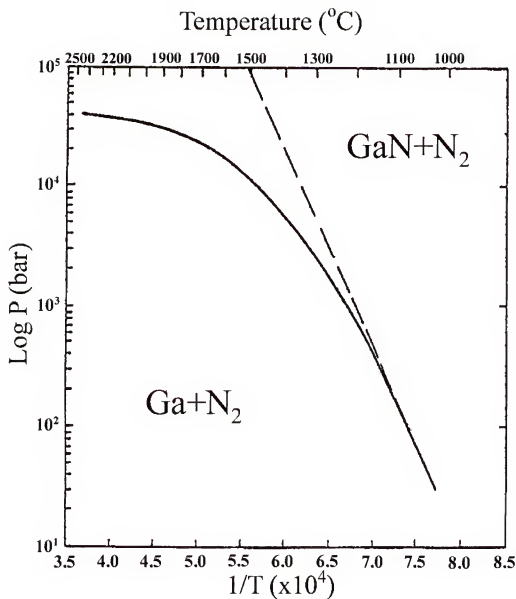
Figure 1-9. Chemical stability of GaN in two different high-pressure systems as a function of pressure and temperature.

CHAPTER 2
EXPERIMENTAL PROCEDURES

Growth and Annealing

The GaN growth and annealing experiments contained within this dissertation, most of which were preformed under high pressure, were carried out using a novel high pressure furnace system, shown schematically with all of its supporting subsystems in Figure 2-1. This quasi-isostatic high-pressure furnace system, or "isopress" was originally designed and built in Russia during the cold war for the purpose of growing gem-quality diamonds. Most of the detailed technical specifications of the high-pressure system not contained herein are proprietary, as the Gemesis Corporation in Gainesville, Florida continues to use this system, and others similar to it, to produce gem-quality diamonds, and also to perform diamond-related crystal growth research in junction with the University of Florida.

Peripheral to this are the various subsystems, including the hydraulic oil pumping system, which consists of a Leeson mechanical pump using Mobil DTE24 hydraulic oil as a medium. The hydraulic pump provides pressurization via the mechanical pumping of oil into the system. Oil is continually pumped into the isopress system until the desired pressure is achieved, and then subsequently the pressure is periodically readjusted to correct for any pressure drop in the line due to oil leakage out of the system, or plastic deformation of solid components inside the isopress.

The second noteworthy subsystem is the AC power supply and control system, which consists of a Neeltran AC power supply and a Gateway PC running the HP-VEE

device computerization control software package, which controls all of the power settings digitally and can be used to program the desired power vs. time profile into the system and maintain the programmed settings automatically. The temperature in the core cell was calibrated as a function of heating element power using a special cell with an Omega "Type G" tungsten/tungsten-rhenium thermocouple inserted in it. The equilibrium cell temperature vs. power profile was measured for the system and this calibrated temperature vs. power curve, shown in Figure 2-2 was used to set the desired temperature in the center of the core cell for all experiments.

The third noteworthy subsystem of the isopress is the heat exchange system, which consists of a Haskris industrial water chiller, a Omnifilter water filter, and various polyvinyl chloride (PVC) plumbing. Water is pumped into the outer die assembly, is heated by the large dies, and flows out through the bottom of the system into the filter, where it is cleaned and returned to the chiller and then recycled into the isopress.

The isopress, shown in Figure 2-3, is the heart of the experimental apparatus used in this research. The isopress consists of an outer chassis of four very large steel pieces, which interlock together to form a sort of clamshell-shaped geometry that is highly stable under tensile loading from the inside. Inside the isopress, several sets of metal dies and gaskets transduce hydraulic pressure from a large spherical outer-shell set of metal pieces and gaskets into a much smaller cubic payload core cell in the center of the spherical isopress.

The oil is pumped into a small spherical-shell-shaped cavity between the outer four large steel pieces and a set of eight octant octant-shaped metal dies, which when assembled together form a large sphere with an octahedral cavity inside it. Oil is

prevented from penetrating inward by a set of hemispherical polymer gaskets that are placed in the outer chassis of the isopress for this purpose. Inward hydraulic pressure is thereby brought to bear on the octant dies and is then transferred inward to a smaller set of six dies, which when assembled form an octahedron with a small hollow cubic volume at its center. These can all be seen in Figure 2-3, but a sketch of the dies is also shown in Figure 2-4 for clarity.

The large dies have small polymeric spacer gaskets glued to them prior to final assembly in the isopress system. These spacers provide a small space between the large dies for the water to flow into and realize effective cooling of the system. Power is supplied to the heating element via a pair copper power feedthroughs, which are placed between the large dies in what would be considered the "poles" of the sphere that the dies form. Power is conducted through these feedthroughs to two of the smaller dies, which conduct electrical power through them in addition to providing effective pressure transduction.

A more conventional electronically-controlled tube furnace was used to provide control samples for the annealing experiments. This was a Lindberg furnace system with an alumina sample tube. The digital control console for the furnace is preprogrammed to ramp the temperature in the "hot zone" of the furnace at a maximum temperature ramp rate of 10ºC/min, though slowed rates are generally observed upon cooling when the temperature goes below about 300ºC, due to a decrease in the cooling rate as the temperature inside the furnace approaches that of the ambient. The furnace tube was sealed on the ends with metal end caps and high-temperature polymer gaskets to prevent

air infiltration during annealing and the tube was flushed with dry argon gas prior to annealing under a small flow of argon.

The core cell at the center of the isopress system is made of various components, and throughout the course of this research many different variations on cell geometry were employed. All of the core cells, however, incorporated a graphite heating element, or "heater" which was used to control the cell operating temperature, and an outer casing, which was made of partially-stabilized zirconia (ZrO_2) and cesium chloride (CsCl). For testing the chemical stability of as-received GaN powder in the isopress environment, a fairly simple cell was constructed using a charge of GaN powder. A schematic diagram of this cell is shown in Figure 2-5. Core cells of this type were used for experiments intended to map out the exact temperatures and pressures under which GaN was stable, and those conditions which resulted in the dissociation of GaN powder into gallium metal and diatomic nitrogen gas.

The core cell configuration used for annealing of thin GaN films grown on sapphire is shown in figure 2-6. These cores were constructed using a small sapphire wafer with a 1 μm-thick layer of MOCVD-grown GaN as the wafer of interest. Placed on top of this wafer was a second, slightly larger wafer, which was made of bare polished sapphire. The second wafer was placed face-down on top of the wafer of interest in an attempt to keep the GaN film surface clean and free of any interaction with the BN which was used to encapsulate the wafers. The boron nitride (BN) components in these core cells were generally machined from BN stock using a <<type and brand>> metal lathe. The outer cell casing was, however, formed out of partially-stabilized zirconia powder, which was first mixed and loaded into a die, then pressed using a Carver uniaxial hydraulic press.

The casing was then sintered in an electronically controlled Lindberg box furnace and, after being allowed to cool, ground to it's desired final dimensions by hand using Buehler grit paper. Finally, the finished casing piece was immersed in liquid CsCl for 30 minutes to allow the CsCl liquid to infiltrate the pores in the sintered body. This CsCl treatment provides added strength, as well as enhancing the desired mechanical properties of the casing relative to untreated sintered zirconia, particularly elastic modulus and compressibility.

By far the most complex and intricate core cell design was that used for growth of GaN bulk crystals from GaN powder and a metal catalyst melt. An example of one of the core cell design configurations is show in Figure 2-7. The bulk growth experiments used many different variations on this design, but this particular core cell was perhaps the most effective. As you can see, many different materials were used in the cell's construction, and when one considers that the total width of the cell was no more than 21mm across, one can imagine how thin some of the wall thicknesses are of some of the component parts which went into the construction. Most of these parts were shaped out of raw ceramic powders, pressed, sintered, and ground by hand to final tolerances, and CsCl treated, using the same techniques as described for the outer casing. The growth core cell incorporates a stainless steel "double cup" structure, which was added to the basic core design in an attempt to alleviate the tendency of the metal catalyst melt to diffuse through the more porous ceramic components and interact with the graphite heating element, which general causes failure of the heater and therefore the experiment. Other experiments did not require this added precaution. One will notice that volume between

the outer casing and the heater is CsCl in this case, which differs from the BN layer used in other cell geometries.

The bulk GaN growth cells, which were constructed and experimented on first, were constructed using older techniques then the later stability and annealing experiment core cells. At the time when the bulk growth experiments were being done, it was the general practice to pack the volume between the heater and the outer casing with CsCl powder in order to ensure that the heater did not touch the casing itself. It was later discovered that machinable BN could be turned on a lathe to form a tubular sleeve with a thin enough wall thickness that this sleeve could be used to replace the CsCl-packing procedure. This sleeve was an improvement over the CsCl packing in that it was a uniform wall thickness all around and facilitated faster and more reliable construction of the cores at the time of final parts assembly.

Characterization

Many different electron beam-based characterization techniques were used to investigate the results of the growth and annealing experiments. As a prelude to discussing the specific techniques, what they each are useful for measuring, and why they were used in this work, it will be useful to have covered the general case of electron beam interactions with matter to form a basis of comparison for the individual techniques used later. Figure 2-8 shows an idealized picture of most of the important electron beam interaction volumes associated with different types of detectible radiation (both particle-like and wave-like) which can be emitted from a sample as a direct result of electron beam bombardment. The figure neglects cathodoluminescence, however, which will be dealt with separately. The exact lateral and vertical resolution of the various techniques are, of course, a function of the beam energy. In Figure 2-8, the beam energies are

assumed to be in the 5-50keV range, which is commensurate with the capabilities of most scanning electron microscope (SEM) systems.

Scanning electron microscopy, or SEM, was performed on samples from both the growth and annealing experiments in the Japanese Electron Optics Laboratories (JEOL) SEM 6400 instrument in M.A.I.C. to measure the size of the GaN crystals grown in the growth experiments, as well as to get qualitative topological information about the surfaces of the annealed samples. This requires a sample that is a least somewhat electrically conductive, which the grown GaN and the annealed GaN films are expected to be, but the sapphire substrates that the annealed samples were grown on are well insulating, so the wafer samples had to be silver painted to the aluminum SEM mount such that the film was well grounded.

Used in imaging mode, the SEM can be configured to detect either the secondary electrons emitted from the sample as a result of the beam (or "primary") electrons, or backscattered primary electrons, which can serve to provide some qualitative compositional information about the sample. We used secondary electron (SE) imaging mode for this work. This was generally done at magnifications as high as 10,000X to determine surface topology of the grown material, but the instrument is capable of magnifications as high as 100,000X depending on beam energy and the electrical properties of the sample. The lateral resolution that the instrument is capable of is at best generally given as ~1nm, but again, this depends on sample and beam parameters. The higher the beam energy, the better the lateral resolution is, but the more current is incident on the sample, which can cause charging of the sample if it is not well grounded or conductive enough to handle the current without Joule heating and beam damage.

The JEOL SEM 6400, like the vast majority of SEM systems it's age, uses a tungsten filament and to produce an electron beam via thermionic emission and subsequent acceleration and beam focusing by a series of magnetic lenses and stigmators. This is shown schematically in Figure 2-10. The electron beam is then rastered across the sample surface area of interest and secondary electron counts are registered in the detector and plotted as intensity on a cathode ray tube (CRT) visual display. The "picture" of the surface thus rendered is of a higher maximum lateral resolution, magnification, and, perhaps most importantly, depth of field, than any optical microscopy technique due to the face that electrons, which have a much shorter DeBroglie wavelength than visible-light photons, are used to image the sample surface.

One characterization technique, which can be, and was, done in situ with the secondary electron imaging, is energy dispersive x-ray spectroscopy, or EDS. This technique takes advantage of atomic excitations that take place as a result of electron bombardment of the sample. Upon subsequent relaxation of the excited atoms back to the ground state, characteristic x-ray emission occurs and this signal can be detected with a charge-coupled device (CCD) detector and an x-ray spectrum obtained. Upon recording of the spectrum, the EDS software can quickly identify most of the peaks recorded and provide the user with a first guess as to what the various spectra are showing. Semi-quantitative compositional analysis is then possible after accounting for spurious peaks, which can occur as a result of CCD artifacts. For example, if a small peak is recorded at exactly twice the energy of another, much larger peak, that smaller second peak will then often be erroneously reported as the presence of an element, when it is actually most

likely a two-photon event being detected by the CCD. This phenomenon is referred to in EDS circles as a "pile-up peak".

The EDS detector can detect all elements on the periodic table with Z   4 and has a lower concentration threshold of about 1-2 wt.%, although lower concentrations can sometimes be detected for heavier elements. Quantification of spectral results into actual concentrations is sketchy without standards, which is the general practice, as other techniques exist for measuring concentrations quantitatively with greater accuracy, such as wavelength dispersive x-ray spectroscopy (WDX). EDS, like SEM is non-destructive, and has a nominal accuracy of ~4-5 wt.% for sample components with in at least 5 wt.% composition. Concomitant with the characteristic x-rays which are produced and detected in the EDS spectrum, there is also usually a brehmstralung background signal which is a result of beam electrons being decelerated n the sample via drag caused by the electron clouds of the sample atoms. Figure 2-8 shows the relative sample volumes from which the characteristic and background x-rays are emitted. EDS measurements were performed on growth samples to investigate composition and detect any impurities that existed in the as-grown material in any detectible quantities, and on the annealing samples to detect any loss of the GaN film upon annealing prior to using other techniques to characterize the films.

Auger electron spectroscopy (AES) is another electron beam characterization technique that was employed in this work to investigate the near-surface chemistry of the grown bulk GaN as well as the annealed films. In the case of the bulk GaN the AES was used to look for any other phases which might have grown epitaxially on the surface of the GaN crystals, as well as to investigate the stoichiometry of the GaN at the near

surface of the crystals. In the case of the annealed films, the AES was employed to investigate any loss of nitrogen near the surface of the films as well as to look for any carbon or oxygen contamination. AES is a technique which involves three atomic electrons and as such can only detect elements with atomic numbers of three or more. The physical basis upon which AES operates was first discovered in 1923 by Pierre Auger and so the technique used today to determine near-surface chemistry of solid samples bears his name.

The beam electron first excites an atom by creating a vacancy in one of the atom's inner energy shells. This vacancy is then filled by a radiationless transition of a higher energy electron down into the vacancy, and the process by which this occurs then imparts the excess energy to another higher shell electron, thus ejecting it and ionizing the atom in the process. The atom is thus left with two vacancies in the upper energy shell which can themselves create further Auger electron emission. The so-called "Auger electrons" thus emitted by the sample can them be collected and plotted as counts versus energy using a cylindrical mirror analyzer (CMA) as a detector. The Auger electrons are generated throughout the tear-drop shaped region in Figure 2-8, but since these electrons are easily re-scattered by the sample before exiting, only the Auger electrons which emanate from depths of within 5-100Å of the sample surface are successfully collected and analyzed.

This gives AES extremely fine depth resolution, and AES from deeper regions can be obtained by sputtering away the sample in order to expose deeper portions of the sample. This process is, of course, destructive, however, and can lead to problems if the various constituents of the sample sputter away at different rates. Because it is so

surface-sensitive, AES must be done under ultra high vacuum (UHV) conditions, and as such requires samples which are UHV compatible. If it is attempted at high pressures than ~10^{-10} Torr, adsorbates on the surface will prevent the instrument from truly probing the sample surface and the only signal that will be collected will be from adsorbed atoms from the gas ambient. The Auger process is only one of a number of processes by which atoms can relax back to the ground state after being excited by the electron beam and x-ray emission, already discussed herein is the other primary process of interest. Figure 2-10 shows the relative probability of Auger emission occurring as a function of atomic number of the sample atom for three different atomic energy shells.

The last, but certainly not least important, of the electron beam techniques used in the work is cathodoluminescence spectroscopy (CL). CL was used because GaN is a material that cathodoluminesces at room temperature and is used in a variety of applications that require cathodoluminescent materials, such as flat panel displays. The basis for CL is that the beam causes an excitation not in the atomic energy levels of the materials atoms, but in the solid-state energy band structure of the material. The beam excites an electron out of the valence band of the material and either into the conduction band, or into a discrete energy level in the mid-gap area. The excited electron then returns to the valence band in any number of radiative and/or non-radiative transitions, and emits one or more photons in the process. One transition, which is usually of interest in any semiconducting or insulating material, is the transition from the conduction band edge to the valence band edge, or the so-called "band edge emission" peak. Precise measurement of this transition energy can then be used to determine the bandgap energy of the material as well, and other peaks near it can be used to determine the positions of dopant levels

which lie near the band edges. Figure 2-11 shows the various energy band transitions that can lead to cathodoluminescence in semiconductors and insulators.

Atomic force microscopy (AFM) was performed on the annealed samples to investigate changes in surface roughness upon annealing of the films. Gallium nitride films tend to roughen due to loss of nitrogen from the surface of the film upon annealing and this is an undesirable effect in GaN device processing. The films annealed in this work were measured with a Nanoscope III scanning atomic force microscope. A diagram of the basic principle of operation of the device is shown in Figure 2-12. The AFM uses a sharp tip, made of Si is mounted on a flexible cantilever. When the tip comes within a few angstroms of the sample surface, repulsive Van der Waals forces between the tip and the sample surface cause the cantilever to deflect.

This cantilever has a laser beam focused on it and when the cantilever deflects, the laser's reflection moves across a solid-state detector mounted in the instrument, which registers the motion of the laser spot on across the detector as movement of the cantilever and as such the topology of the sample can be mapped out by scanning the tip across the surface. AFM is nondestructive and can have lateral resolutions capable of imaging separate atoms, given a smooth enough surface and good vibrational isolation of the equipment. For rougher surfaces, the lateral resolution is generally around 1nm however. The vertical resolution of the instrument can be as high as 0.01Å. The AFM instrument is equipped with a computerized control system which both renders the surface map image in a number of different color and grayscale representation schemes, which can be useful for different applications. The control software is also capable of automatically calculating the roughness of the samples from the data collected and be used to report on

the surface Rms roughness, tortuosity, peak-to-peak roughness, and many other figures of merit useful for fractologists, electronic materials scientists, and surface scientists.

X-ray diffraction (XRD) techniques of various kinds were used in this work to investigate both the bulk grown GaN samples and the annealed film samples. In the case of the former, XRD was employed to investigate the phase of the material grown, both to ensure that GaN was in fact the material produced, to determine which of the two known phases of phase of GaN was generated by the growth experiments, and to gain at least qualitative information about the crystalline quality of the material. In the case of the latter, GaN films annealed under high pressure and under flowing argon were probed to determine any microstructural changes in the films upon annealing, relative to untreated samples. Rocking curves of two kinds, Ω-only and Ω-2θ, were performed on the annealed film samples to determine at least qualitative information about the effects of the annealing experiments on the degree of tilt mosaicity in the samples as well as any changes in the d-spacing of the planes investigated. XRD on the bulk grown GaN material was performed using a Rigaku Cu rotating anode target, a singly-bent (vertical focusing) LiF monochromator, and a four-circle Huber diffractometer (standard 2θ, θ, χ, and φ circles), whereas the characterization of the annealed films was performed at the M.A.I.C. facility using a Phillips X'Pert high-resolution x-ray diffractometer.

Bragg's law of diffraction, the basic principle upon which XRD systems operate, is shown in Figure 2-13. A beam of monochromic, collimated x-rays incident on the sample is diffracted by the atomic planes of the sample and the direction into which the x-ray signal is reflected is dependant on the lattice spacing of the sample atomic planes through the Bragg relation:

$$n\lambda = 2d\sin\theta \qquad\qquad (2\text{-}1)$$

where θ is the angle of incidence of the x-ray beam, d is the lattice spacing of the planes involved in the diffraction, λ is the wavelength of the incident x-ray beam, and n is the diffraction order, which is generally equal to 1 for most experiments, as higher order diffraction spots are generally of much lower intensity.

Raman spectroscopy was used on the bulk grown GaN samples to help to positively identify them as wurtzite GaN. Raman spectroscopy can be used to determine structural properties of materials and works by measuring the vibrational spectra of sample atoms. The Raman spectrometer system uses a laser to generate an intense beam of monochromatic light, which, when incident upon a sample, causes the electron clouds of atoms to distort, storing some energy, just as a compressed spring stores energy. When the light wave passes and the electron clouds relax, the stored energy is reradiated. Most of this reradiated energy is emitted at the same frequency as the laser used in the system, which is a phenomenon called Rayleigh scattering, but a small portion of the energy stored by the distorted electron cloud is transferred to the sample itself, thus exciting vibrations in the chemical bonds between the atoms which make up the sample. The energy of a vibration is therefore deducted from the laser energy and a spectral peak will appear in the spectrum at a frequency less than that of the laser. Such a peak is called a Raman line and the frequency difference between this Raman line and the laser frequency is directly representative of the vibrational frequency excited in the sample.

The opposite process can also occur where a lattice vibration annihilates with the laser beam, thus adds to the energy of the laser, and a peak appears at a higher frequency than that of the laser. The intensity of this second type of Raman line, since it is

dependant on thermally activated vibrations to be present in the sample a priori, is strongly temperature dependant, and are therefore of less general usefulness than the only weakly temperature-dependant first variety. Figure 2-14 shows a schematic representation of a common Raman spectrometer system. Raman spectroscopy owes it's existence to the invention of the laser, though the phenomenon was known about before the laser was invented, as the laser makes intense, highly monochromatic light much easier to produce in the laboratory and as such makes Raman spectroscopy much more readily available.

Photoluminescence spectroscopy (PL) was performed on the annealed film samples to investigate the effect of the annealing on the PL spectrum itself and to determine if any optically active impurities were created in the annealing process. The basic principle of photoluminescence is that some materials, which are called luminescent, will absorb incident photons by the promotion of an electron in the material from one (lower) energy state (or band) to another, higher energy state or ban, and after some relaxation time, the electron will return to the lower state and emit a photon as it does so, by a process called radiative recombination.

Not all materials exhibit radiative recombination at all temperatures and materials which do exhibit it are called luminescent materials. Studying the exact frequency of the luminescence form the material as well as the relaxation time can provide about the material itself, including bandgap energy, energy levels of impurities in the gap, doping density, electron temperature, and expected lifetime of excited states. Direct bandgap semiconductors like GaN are often used for light-emitting diode and laser diode applications and as such PL is a valuable tool for probing many of its important optical

and electronic properties. The instrument used to perform the PL measurements on the samples in this work is shown schematically in Figure 2-15.
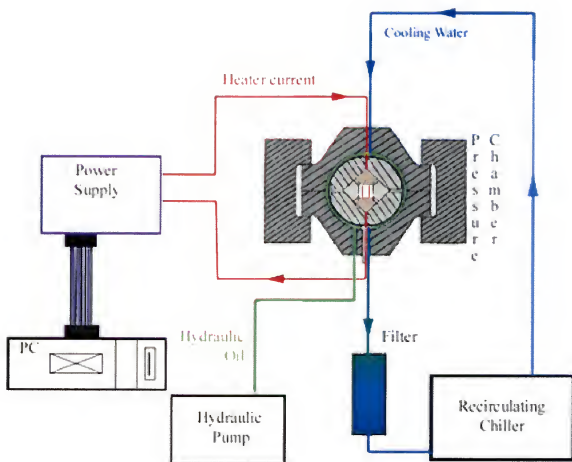
Figure 2-1. High pressure system and its subsystems.
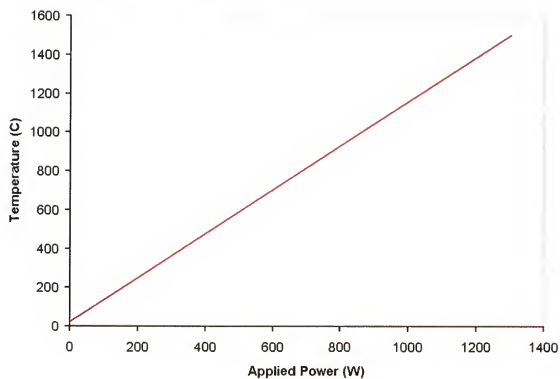
Figure 2-2. Cell temperature versus applied power.
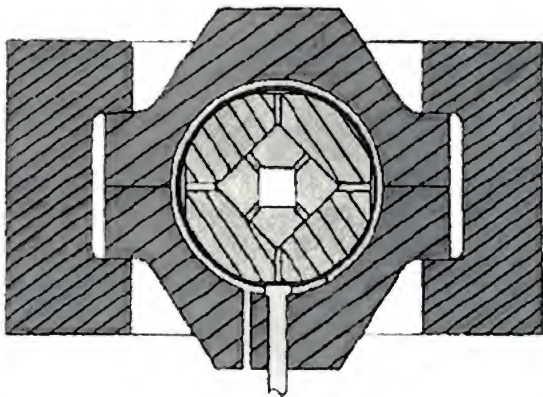
Figure 2-3. Isopress system.
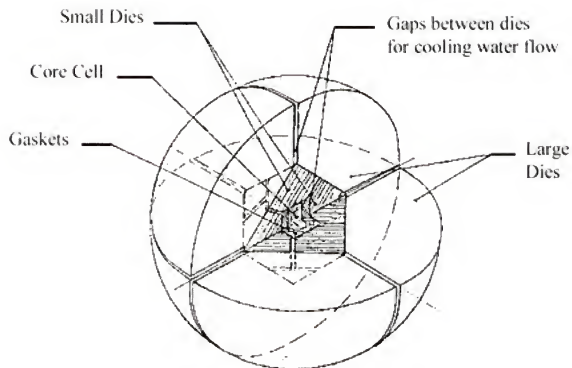
Figure 2-4. Two sets of metal dies.

ZrO/CsCl   GaN

Graphite   BN
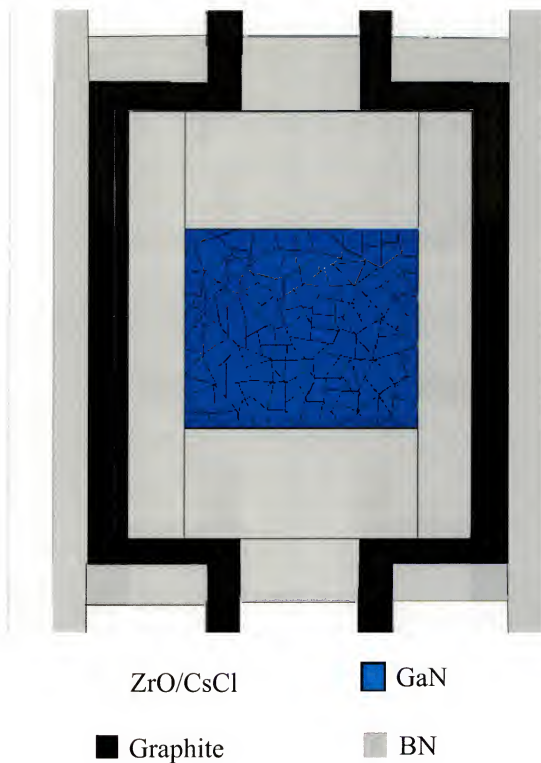
Figure 2-5. Cell geometry used to measure the chemical stability of as-received GaN powder in the isopress.
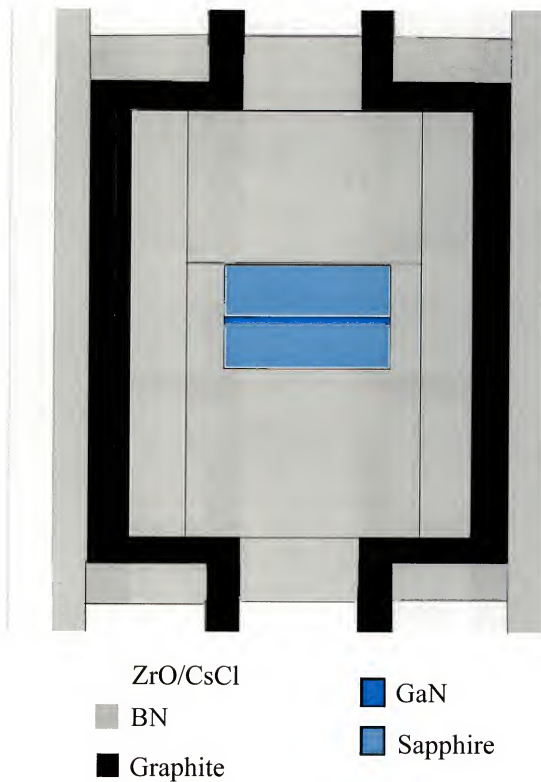
Figure 2-6. Cell geometry used for annealing GaN films in the isopress.

▨ MgO	▨ ZrO/CsCl
▨ Stainless Steel	▨ CsCl
▨ 0.8CsCl/0.2BN	☐ GaN
■ Graphite	▨ 0.7Ga/0.3Mn
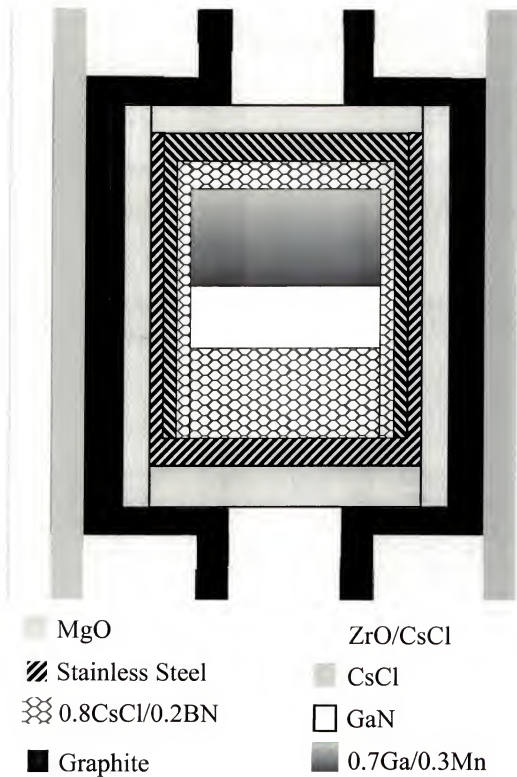
Figure 2-7. Cell used for bulk GaN growth.
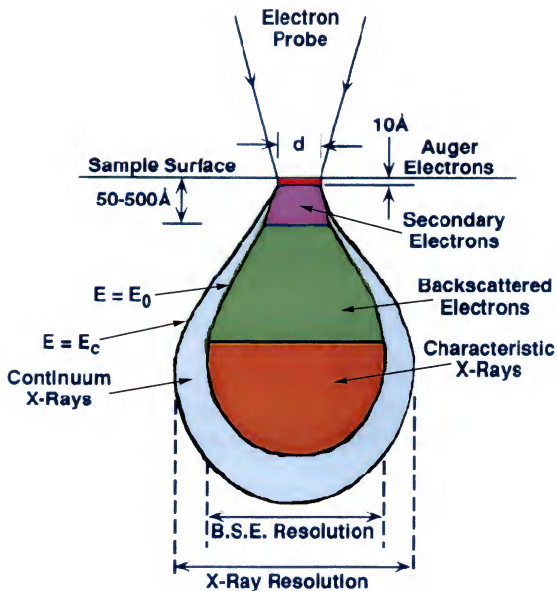
Figure 2-8. Electron beam interactions with solid samples.
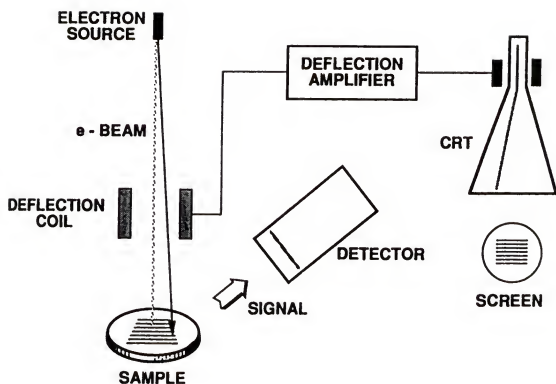
Figure 2-9. Basic SEM apparatus.
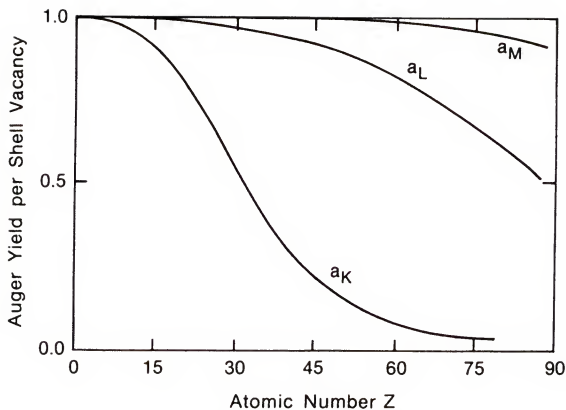
Figure 2-10. Percentage of inner shell vacancies resulting in Auger electron emission for holes in the K, L, and M shells.
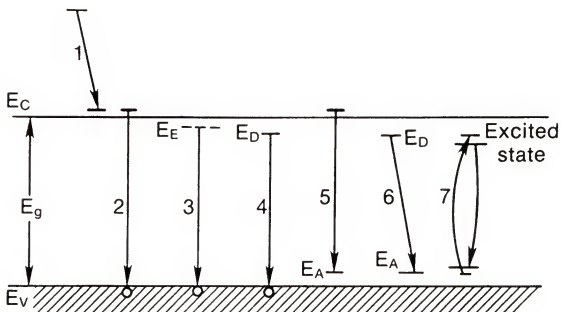
Figure 2-11. Cathodoluminescence transitions possible in semiconductors and insulators.
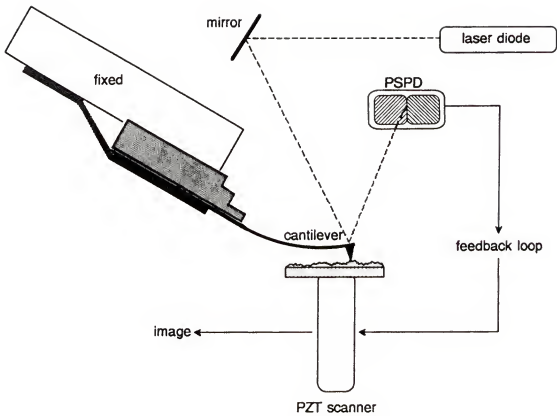
Figure 2-12. Basic scanning AFM instrument.
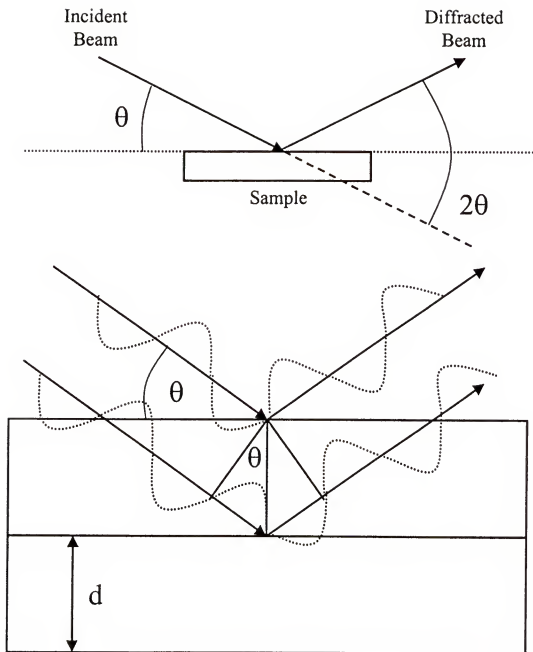
Figure 2-13. The basic principle of x-ray diffraction obeying Bragg's Law.
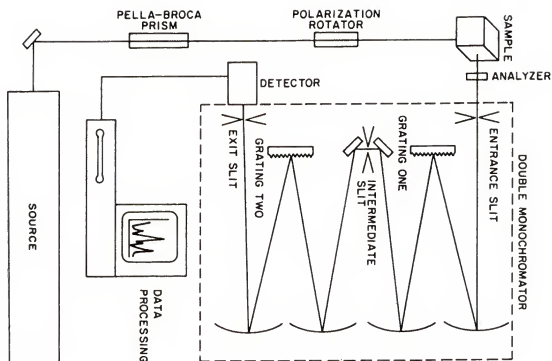
Figure 2-14. The basic Raman spectrometer system.
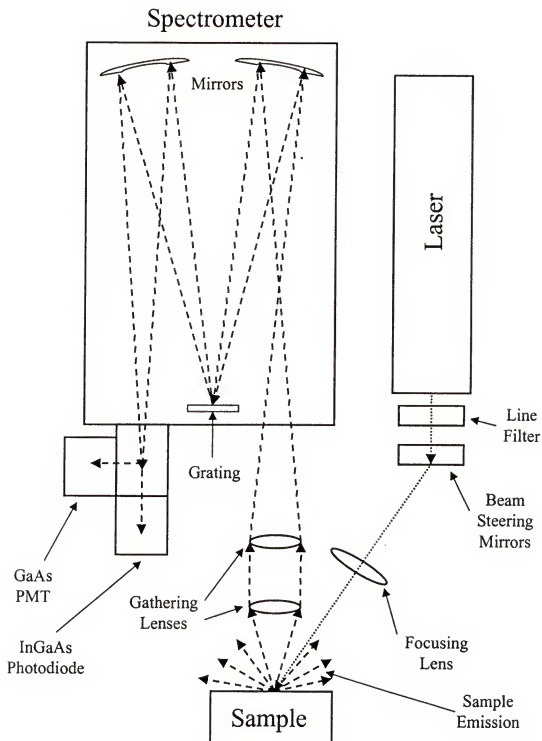
Figure 2-15. The PL system used in this work.

CHAPTER 3
EXPERIMENTAL RESULTS AND DISCUSSION

This chapter discusses the results of the experiments conducted as part of this scientific investigation. These results are discussed in more detail in later chapters.

Thin Film Annealing Experiments

Prior to conducting any annealing experiments in the isopress system, the system was tested to determine what experimental conditions would preserve GaN powder and which conditions would allow the GaN powder charge to degrade into Ga meatl and N-containing gasses like ammonia and diatomic nitrogen. The results of a selected group of these GaN stability experiments are shown superimposed onto the GaN-N thermodynamic phase diagram in Figure 3-1. The results seem somewhat illogical until one considers that the isopress system is not a "closed system", that is, it isn't air-tight, until a pressure of at least 32-35 kbar is reached. At pressures below this threshold, the dies and gaskets will allow gaseous reaction by-products to escape into the cooling water flow lines. All stability tests were conducted at a heater power throughput of 1300W, which corresponds to an inner-core temperature of 1500 C $\pm$ 25 C in the reaction zone.

Two 2" diameter wafers were obtained which consisted of a 1 μm-thick layer of P^{+} GaN grown by MOCVD on (0001) oriented sapphire (αAl$_2$O$_3$) substrates. The back surface of each wafer was unpolished and had a 1micron layer of tantalum sputter-deposited on to the wafer to enhance thermal uniformity across the wafer surface during film growth. The wafers were cleaved along the (10-1 0) and (1 2 -3 0) directions into square samples roughly 5mm on a side. These samples were then polished on a grinding

wheel to remove the square corners of the samples and to smooth the cleaved edges of the samples, in order to reduce the tendency of square samples to chip near the corners and edges. The samples were handled with gloved hands throughout the grinding process and cleaned with methanol after grinding in a Pyrex beaker in an ultrasonic cleaner. Each sample was then loaded into it's core cell as part of the final assembly process of the core cells and the core cell then loaded into a Forma Scientific vacuum oven at 140ºC for 24 hours to eliminate any moisture prior to being loaded in the high-pressure system. The pressure system was then purged with dry nitrogen (99.99 pure) for 120s to force out as much ambient air as possible before pressurization. After the high-pressure system reached the desired pressure, in this case ~45 ±2 kbar, an AC current was then applied to the graphite heating element inside the cell. This current was adjusted by programming the desired voltage across the heating element, using the HP-VEE laboratory software package to control the Neeltran power supply. The heater voltage and current were then read off of analog volt and amp meters on the Neeltran's front console. The heating element develops a temperature in the sample zone, which is measured to be linear function of the applied heater power. The slope of this line was calibrated and the power set to the temperatures of interest in each case. The power was ramped manually by adjusting the heater voltage and the average ramp rate was kept around 10ºC/min.

The control samples which were annealed in a conventional furnace at ambient pressure were first cleaved from the stock wafer, cleaned in methanol, allowed to dry in the laboratory, and loaded into a digitally-controlled Lindberg tube furnace with an alumina sample tube. The air in the tube was first flushed out with argon and then the annealing experiments were carried out in the hot zone of the furnace under a 10ml/min

continuous flow of argon for the same times and temperature as the high-pressure samples. The temperature was ramped up to the desired temperature at a ramp rate of 10ºC/min, controlled by the Lindberg digital furnace controller.

The samples recovered from the annealing experiments were mounted to individual aluminum slides for the purposes of sample characterization. This slide-mounting step provided additional protection to the samples themselves, as once they were mounted to the slide, they could be easily handled by touching the slide only. The samples annealed under flowing argon were ultimately demounted from their slides and mounted together on a single aluminum SEM mount acquired at M.A.I.C., again using silver paint. The samples annealed under high pressure were however left on their slides and a second set of wafer chip samples was mounted to a second SEM mount for SEM and CL purposes.

Scanning electron microscopy imaging was performed on the annealed samples to investigate, qualitatively, the surface quality of the samples upon annealing and to ascertain the extent to which any of the samples was damaged in any way. All SEM characterization was performed in the JEOL SEM 6400 microscope in M.A.I.C. As mentioned previously, there were two sets of samples, and each was mounted to an aluminum SEM mount. One set contained the samples annealed under flowing argon and an as-received sample, and the other set contained all of the samples annealed under high pressure and an as-received sample. All of the SEM images were recorded at an accelerating voltage of 15keV and with the condenser lens set to 9 which corresponds to a beam current of 1×10^{-10} A.

Figures 3-2, 3-3, and 3-4 show SEM images taken from an as-received sample, the sample annealed under high pressure at 1100ºC, and the sample annealed under flowing

argon at 1100ºC, respectively. Note that the high-pressure annealed sample image exhibits more surface damage, which is attributed to several factors. First, the isopress system, though it approached a quasi-isostatic pressure ambient, is imperfect and still retains some asymmetry in the pressure exerted on the core cell. This pressure irregularity can lead to strain of the sample and as such the samples have a tendency to develop small cracks in them. Second, the presence of BN powder between the top wafer and the film wafer in the cell can lead to small digs in the film surface which are inherently unavoidable with this technique given the core cell fabrication and assembly procedures which must be used. Lastly, some of the samples, particularly the sample annealed under high pressure at 900ºC (see Figure 3-5) exhibit streak lines, which are either parallel or at 120º angles to each other. This can be attributed to slip of the monocrystalline sapphire substrate under pressure loading at elevated temperature. Other examples of this type of slip system behavior have been reported in the literature for sapphire [85, 86] with slip being reported for sapphire oriented for prism plane slip at temperatures as low as 200ºC.

Figures 3-6, 3-7, and 3-8 show EDS analysis of an as-received sample, the sample annealed under high pressure at 1300ºC, and the sample annealed under flowing argon at 1300ºC. Although some evidence of oxygen and aluminum peaks is starting to show in the high-pressure sample, it should be noted that there is still significant evidence gallium and nitrogen as well, whereas in the data representing the sample annealed under flowing argon at 1300ºC, there is absolutely no evidence of any remaining gallium or nitrogen in the sample. The fact that the high-pressure annealed sample shows some aluminum and oxygen in the EDS spectrum is indicative of two things: one, that the film is damaged and some substrate area is exposed to the electron beam, and two, that the film may be thinner

than the film on the as-received sample, and some electron beam penetration to the substrate beneath is possibly evident.

AFM topographical images and measurements of Rms roughness performed on each sample annealed as well as an as-received sample for purposes of comparison. All AFM characterization experiments were conducted at the Engineering Research Center for Particle Science and Technology using an SPM Nanoscope III atomic force microscope which is owned and maintained by the M.A.I.C. at the University of Florida. All of the AFM procedures discussed in this work were taken on $1\mu m$ x $1\mu m$ square area of the samples, with the instrument configured in tapping mode and using the size E scanner head, and at a scan rate of 3.05 Hz, which is the recommended frequency for the area size sampled. The AFM probe tip was re-tuned before each scan was attempted, and after each sample scan, the data was digitally manipulated by first performing a first order plane fit (called "Plane Fit Auto" in the software) followed by a first order "Flatten" operation. These two operations have the combined effect of digitally removing any gross sample tilt angle from the data acquired, which is usually a very necessary precaution, due to the fact that flat thin film samples are nearly impossible to get completely physically level with the instrument.

Figures 3-9 through 3-12 each show a pair of topographical AFM images acquired at each temperature in used in the study, with the image on the left indicating the data taken from the high-pressure sample and the image on the right indicating the data taken from the high-pressure annealed sample in each case. In almost all cases, the sample annealed at each temperature under high pressure can be seen to be smoother than the sample annealed at the same temperature under flowing argon. These images represent

the lowest roughness data scan from each sample at the temperature indicated, and the images clearly show that the high-pressure sample is an order of magnitude (or more) smoother than the sample annealed under flowing argon, with one exception, the samples taken at 1000ºC.

Figure 3-13 shows a plot of annealed sample roughness values versus annealing temperature for the two different annealing techniques. While the high-pressure annealed samples all exhibit Rms roughnesses of less than 10nm, with most samples well below that, the Rms roughnesses of the samples annealed under flowing argon show a dramatic increase in Rms roughness starting near 1100ºC. It should also be noted that the sample which was annealed under flowing argon at 1300ºC has no data point, owing to the fact that the film was lost entirely in that experiment, and as such no roughness measurement was performed on that sample, as the roughness measured would only be indicative of the substrate itself and/or and residual oxide or nitride layer formed during the anneal and not the desired GaN film. It should also be noted that these Rms roughness values represent the best (smoothest) roughness attainable from each sample.

The furnace annealed samples exhibited similar surface features across the entire sample, but the high-pressure annealed samples were less uniform across the sample surface, owing to the tendency of the quasi-isostatic high-pressure loading to cause stresses in the samples and subsequent slip of the sapphire substrate along the prism planes under temperature and pressure conditions used in the study. Also, due to the fact that the core cells are composed of processed ceramic powder components, the presence of any unwanted grit in between the GaN film sample and the bare sapphire sample used as a protective cover can cause digs to appear in the GaN film upon recovery of the

samples from the isopress annealing reactor. In the case of the high-pressure annealed samples then, the Rms roughness reported are from the most well preserved areas of the sample surface visible under the optical system of the AFM instrument, and not from the areas that exhibit significant slip lines or pressure-related surface damage.

X-ray diffraction spectra were taken from a sample from each annealing experiment, as well as an as-received sample, using a Phillips X'Pert x-ray diffractometer with a fixed x-ray beam source operating at and x-ray wavelength of 1.540560Å, a rotatable detector arm with a flat crystal monochromator detector and a sample stage with three axis rotation and three axis translation capabilities. All x-ray diffraction spectra were taken at an x-ray source voltage of 45kV and a source current of 40mA. All spectra were scanned over an angular (2θ) range from 5 to 70 degrees, which is the maximum angular range of the instrument. Each sample was mounted to a small aluminum slide using silver paint, this procedure made the samples easier to transport to the various characterization instruments used in this work. In some cases, particularly the samples annealed under high pressure, the samples scanned were narrower than the width of the x-ray beam and as such, great care was taken to align the samples prior to the spectral scans.

Figures 3-14, 3-15, and 3-16 show the spectra taken from an as-received sample, a sample annealed at 1300ºC under high pressure, and a sample annealed under flowing argon gas at 1300ºC, respectively. Note that the GaN (0002) reflection at $2\theta \sim 34.5º$ is present in both the as-received sample scan and the high-pressure sample scan, but not in the sample annealed under argon flow. The reflection at ~43º visible in all three spectra, and most prominent in the argon annealed sample spectrum correlates well to the known

(0006) reflection of the sapphire substrate, and the other reflections visible in the first two spectra (Figures 3-14 and 2-15) at ~38°, ~65° and ~45° can all be attributed to known aluminum reflections which we can surmise are visible due to the fact that most of the samples were narrower than the x-ray beam width and therefore some areas of the bare aluminum slides which the samples were mounted onto was exposed to the x-ray beam and thus the peaks are visible.

Each of the other samples, all of which exhibited a prominent GaN (0002) reflection at ~34.5°, was scanned using the same Phillips X'Pert system, this time using a triple-axis multi-crystal detector which has a higher maximum angular resolution than the flat crystal monochromator used in the XRD spectra scans, in order to obtain an Ω-scan rocking curve for each sample. This analysis is usually performed on textured thin film samples in order to determine the relative amount of tilt mosaicity of the films analyzed, by analyzing the full width at half maximum (FWHM) of each rocking curve. The stacked graphs in Figures 3-17 and 3-18 show the Ω-scan rocking curves for the high-pressure annealed samples and the samples annealed under flowing argon gas, respectively, with each curve superimposed onto one graph in each case.

Note that the peaks in each curve do not necessarily line up on the same absolute angle value. This is explained by the fact that the samples were all mounted to aluminum slides with sliver paint and as such, small angular corrections had to be made in the omega axis to get each sample aligned with the detector, the gross shift of the peaks relative to each other is therefore inconsequential, as it only amounts to a correction in the alignment of the omega axis rotation of the sample on its own absolute scale, and not to any meaningful deviation of the tilt of the GaN film grains relative to each other.

What is of noteworthy consequence is the noticeable broadening of the peaks annealed under high pressure, and the seeming multiplicity of the peaks into several smaller maxima localized around each other. This is explained by the fact that the high-pressure sample wafers underwent some fracturing during the annealing process and also exhibited significant slip along the prism planes of the sapphire substrate. Both of these factors can lead to the disjointed Ω-scan rocking curves seen here, as both can lead to physical tilting of one area of the wafer relative to another. Figure 3-19 shows a plot of the FWHM values measured for each of the scans shown in Figures 3-17 and 3-18. Not surprisingly, the high-pressure experiments show much larger FWHM in general than the samples annealed in flowing argon gas, and not surprisingly, there is considerably more scatter in the FWHM values as well, due to the fact that the fracture and slip processes which are most largely responsible for the FWHM of the high-pressure samples are somewhat dependant on the exact size, shape, and orientation of the individual samples and also on the exact nature of the anisotropy in the pressure transduction system of the isopress itself.

Similar, $\Omega/2\theta$-scan rocking curves were also performed on each sample, in an effort to determine any changes in the spread in lattice spacing of the GaN by determining the FWHM of the rocking curves. The FWHM of the rocking curve measured in the $\Omega/2\theta$-scan rocking curve experiments can be directly related to the spread in d-spacing of the reflection studied, in this case the GaN (0002) reflection, via Bragg's law. It should be noted here that, in theory, only 2θ need be varied in order to determine the d-spacing changes in the sample, but as this would require moving the x-ray source, the usual techniques is instead to leave the source fixed and rotate both the sample and the detector

to achieve the same effect. Unfortunately, this also requires careful optimization of all the scan angles and, as such, the same problem of relative peak shifting is encountered here as in the Ω-scan rocking curves previously shown. The scans are made by varying both the detector angle and the sample tilt angle and as such the only angle which is varied in the Bragg picture is 2θ, however, when configured to measure rocking curves in this mode, the X'Pert records not the value of 2θ but instead the value of Ω as the abscissa for the scan, and as such the relative shift of the gross sample tilt due to the mounting procedures creeps in again.

Figures 3-20 and 3-21 show $\Omega/2\theta$-scan high resolution XRD curves for the high-pressure annealed samples and argon-annealed samples respectively, again superimposed upon each other for purposes of comparison. Figure 3-22 shows a plot of the FWHM values obtained from these rocking curves as a function of annealing temperature for the two methods described. Note that while the high-pressure samples exhibit higher FWHM values (and therefore more spread in the d-spacing of the GaN (0002) planes) than the argon annealed samples values, the trend lines would appear to have differing slopes, with the slope of the high-pressure annealed samples being the shallower of the two. One can extrapolate from this that, were the GaN film not completely evaporated upon argon annealing at 1300ºC, the trend lines would cross at higher temperatures. As it is, the argon-annealed data set is missing a 1300ºC data point, but the high-pressure set is not, since the high-pressure process exhibits a preserved GaN film upon annealing at that temperature. The reason for the increased FWHM of the high-pressure annealed samples is however still not evident from the data presented.

Photoluminescence spectroscopy (PL) was performed on selected samples by Dr. Mark Overberg at the University of Florida in order to investigate the effects, if any, of the high pressure anneals on the bandgap and optically active impurities. The photoluminescence spectrometer instrument used for all PL spectra has an operating range from 335 to 850nm in wavelength that the detector can reliably detect, and uses a He-Cd laser operating at 35mW at a wavelength of 325nm to excite photoluminescence in the sample. The experiments were carried out at a set of temperatures ranging from 300K to 5K by cooling the evacuated sample chamber with flowing liquid helium. For several of the experiments, attenuating optics were used to avoid saturating the detector, since the PL signal from two of the samples was intense enough to make this a real possibility at lower temperatures. Two samples, the ones annealed under high pressure at 1100°C and 1200°C, were selected for PL characterization at temperature of 300, 200, 100, 50, and 5 Kelvin, in that order and one as-received sample was scanned at 300 Kelvin.

Figure 3-23 shows the PL spectrum of the as-received sample, which exhibits a prominent band-edge feature that peaks at 363nm and tails off completely around 500nm. Band-edge peaks are normally of this asymmetric shape, with a sharp cutoff at shorter wavelengths (higher energies) and an exponential tail toward longer wavelengths (lower energies). The reason for the sharp cutoff at higher energies is that any electron promoted from the valence band of the material into an empty energy state in the conduction band will generally migrate to the conduction band edge via non-radiative processes and then, ultimately, recombine radiatively with a hole in either the valence band or any mid-gap states available. Figures 3-24 and 3-25 show the five PL spectra

taken from each of the high-pressure annealed samples that were investigated in the instrument. There are three prominent features present in both sets of spectra. The broad feature in the spectral range between 525nm and 700nm in both sets of spectra is a yellow luminescence feature often found in GaN, which can be attributed to carbon impurities or gallium vacancies in the GaN film.

The somewhat narrower peak at ~ 400nm in both spectra are most likely the result of radiative recombination associated with near-band edge states in the bandgap involving either conduction band edge to acceptor state recombination or donor to valence band edge recombination. The less intense, somewhat wider features at ~800nm in both sets of spectra can also be attributed to the same recombination processes responsible for the peak at ~400nm, since the spectrometer uses a diffraction grating to produce the sample spectrum. A radiative recombination which produces a photon at ~400nm can then be diffracted off of the spectrometer's diffraction grating via a second order diffraction event and be scattered into the detector as it sweeps the ~800nm range of wavelengths when in fact the light is NOT truly 800nm in wavelength but has been diffracted at the same angle into which an 800nm photon would be diffracted. The spectrometer diffraction grating obeys the diffraction condition:

$$n\lambda = 2d\sin\theta \qquad\qquad (3\text{-}1)$$

where n is the diffraction order of the scattering, d is the slit spacing of the diffraction grating, θ is the angle that the light is diffracted into, and λ is the wavelength of the light diffracted. As the detector sweeps through the angle θ it records only the intensity of the light incident upon it, and not truly the wavelength, so as such the spectrometer is constructed assuming only first order (n=1) diffraction events and can lead one to

misleading conclusions unless one takes into account the possibility of second order (n=2) diffraction condition events which can occur.

Since there is a large peak at ~400nm, one can expect there may well be a weaker second order diffraction peak at "800nm" in the spectrum, which is actually a 400nm signal diffracted into the same angle that a true 800nm photon would be diffracted into. The spectrometer can only really measure the angle at which the light is diffracted, and as such it labels the second order diffraction as being of 800nm wavelength, when in fact it is quite probably of 400nm wavelength. The two spectral features (the peak at ~400nm and the peak at ~800nm) are also strongly dependant on temperature and follow each other quite closely in their temperature dependence. Both peaks are at their most intense at the same temperature (50K for the 1100°C annealed sample, 5K for the sample annealed at 1200°C) and the relative intensities at the other temperatures follow each other quite closely up and down the temperature range over which the PL spectra were taken.

Cathodoluminescence spectra (CL) were recorded for several of the high-pressure annealed samples by Dr. James Fitz-Gerald at the University of Virginia. The CL spectrum of any GaN sample is of great importance in and of itself, as GaN is useful for applications that make use of the cathodoluminescence effect directly, such as field emission displays. The CL technique is a complementary technique to PL as both excite electrons in the band structure of the GaN film and measure the wavelength (or energy) of the photons emitted via radiative recombination processes, which take place upon relaxation to a more energetically favored state.

Figure 3-26 shows a CL spectrum taken from an as-received GaN film sample. This spectrum was taken in an SEM instrument equipped with a CL detector, the magnification of the SEM was set to 250X during the sampling of the CL spectrum shown, with a beam accelerating voltage of 15 kV, an emission current of 20μA, and an absorbed current of $4x10^{-10}$A. The working distance of the SEM instrument was 7.8 mm. The CL scan itself was conducted over a range of wavelength from 300 to 800nm using 1nm steps with a dwell time of 2s at each step. The spectrum shown in Figure 3-26 exhibits a well-defined band edge emission feature at ~3.4 eV and is otherwise unremarkable. Figure 3-27 shows a CL spectrum taken from the sample annealed under high pressure at 1100°C. This spectrum was taken in the same SEM instrument at the same magnification as the as received sample, with the same beam voltage, emission current, absorbed current and at the same working distance. The CL spectrum scan was taken over a range from 200 to 800nm this time, using 1nm steps but with a dwell time of only 1s per step. Despite the fact that the scan was quicker in this case the noise level in the spectrum appears lower, due to the fact that the emitted CL signal in this case was an order of magnitude more intense at it's apex than the as-received sample was at its apex. The spectrum in Figure 3-27 shows a prominent yellow emission feature at ~2.25eV, which supports the PL, feature at the same energy. Both CL procedures were conducted at room temperature (~300K) and with a photomultiplier (PMT) high-tension setting of -960V and in each case the intensity values, which are in arbitrary units, were sampled 75 times at each wavelength and the intensities then averaged.

While the data presented herein clearly show that the high pressure process has been successful in suppressing the tendency of GaN to dissociate upon high-temperature

annealing, other factors which degrade the GaN films in other ways are also observed to occur, such as the pressure induced slip of the sapphire substrate at elevated temperatures, and the tendency of grit between the film and the cover wafer to cause abrasion of the film surface during annealing. Carbon from the heating element is most likely the cause of the increased yellow emission in the films and also the increase in the FWHM of the x-ray rocking curves from the samples annealed under high pressure.

Bulk Growth Experiments

Forty-seven different experiments were conducted to investigate the efficacy of GaN bulk growth under high pressure in the isopress system. Many of these experiments yielded non-remarkable results however, due to a myriad of processing difficulties and unforeseen problems. Some experiments destabilized after a short time at the desired process pressure and temperature, and others, which remained stable, saw little or no dissolution of the source GaN powder charge upon recovery from the isopress system. The reactor core cells were modified for increased performance after each experiment and two of the most successful experiments were selected for characterization and analysis upon careful inspection of the recovered core cell contents. The earliest experiments were conducted by Dr. Robert Chodelka and Dr. Alexander Novikov at the University of Florida, and the later 36 experiments were performed by Dr. Donald R. Gilbert and the author. Core cells from other experiments yielded similar GaN crystals as well, but the data shown here represents a good cross-section of the most meaningful and interesting data collected in this work.

The first noteworthy experiment was conducted using a core cell of the geometry depicted in Figure 3-28. For this work, the cell contained a pressed GaN powder pellet charge, which acted as a source of nitrogen upon heating, and pure (99.99%) Ga metal as

reactants. Crystal growth proceeded by first applying compressive mechanical loading of the reactor core to the desired pressure level of 1700atm, after which the cell temperature was ramped up to the desired value of ~1450°C ± 50°C by setting the heating element power to 1251W (see the thermocouple calibration curve, Figure 2-2 in Chapter 2). Time-dependent heater power profiles were preprogrammed and controlled by computer. The process remained stable and was arrested after 36 hours. After processing, the reaction cell was extracted from the reactor, opened, and the remaining Ga metal dissolved in an HNO3/HCl acid solution, leaving the GaN crystals available for collection and analysis. Crystal morphology was evaluated using SEM, while structural characteristics were evaluated using X-ray diffraction (XRD) and micro-Raman spectroscopy.

Multiple GaN crystals were formed during the course of each experiment as a result of spontaneous nucleation in the Ga metal melt under the conditions used. SEM micrographs of crystals synthesized in this UHP process are shown in Figure 3-29. These crystals exhibit plate-like morphologies suggestive of a hexagonal structure and are ~600 - 800 mm in size. Small (~10 μm) triangular growth features visible on the faces of the crystals displayed preferential orientation with respect to each other, suggesting either single crystal or highly textured growth. Dendritic and needle-like crystals were also commonly observed after processing. Energy dispersive X-ray spectroscopy (EDS) shown in Figure 3-30 gives semi-quantitative analysis, which indicates that crystals formed in this process tended to be nitrogen deficient (N/Ga<1).

Structural characterization of the crystals was accomplished using XRD and micro-Raman spectroscopy. XRD was performed using a Rigaku Cu rotating anode target, a

singly-bent (vertical focusing) LiF monochromator, and a four-circle Huber diffractometer (standard 2θ, θ, ω, and ϕ circles). The XRD spectrum analysis, shown in Figure 3-31, shows the sample to be single-crystal hexagonal GaN with the broad face oriented parallel to (0001). The measured lattice parameters were: a=3.19 D and c=5.186 D, which are in good agreement with published values for GaN. A θ-scan rocking curve taken about the (0004) plane from this crystal is shown in Figure 3-32. The quality of the crystal was such that the rocking curve full-width-at-half-maximum (FWHM) was no wider than the resolution limit (108 arc sec) of the spectrometer, indicating a low defect density crystal. Acquisition of a ϕ-scan showed the (1 0 -1 0) planes spaced at regular 60° increments, further verifying the hexagonal structure, as shown in Figure 3-33.

A micro-Raman spectrum taken from the same crystal is shown in Figure 3-34. The Raman spectrum was taken in a backscattering mode using the 514 nm line of an Ar-ion laser at a spectral resolution of ~1 cm-1. This spectrum shows the characteristic transverse optic (TO) and longitudinal optic (LO) modes of wurtzite GaN, marked A1(TO), A1(LO), and E2 at Raman shifts of 528, 730 and 565 cm^{-1}, respectively. Asymmetry in the E2 phonon mode peak was the result of a small, unresolved E1(TO) mode peak at ~554 cm-1. The A1(LO) and E2 modes are the theoretically allowed modes in the backscattering geometry. Presence of the weak A1(TO) mode in the spectrum may be indicative of an imperfect backscattering alignment during spectral acquisition.

The second experiment of noteworthy merit was conducted using the reactor core cell configuration shown in Figure 3-35. This reactor core cell has two major improvements over the core cell of the earlier experiment shown in Figure 3-28. First,

the reactor core cell has a stainless steel "double cup" capsule encasing the reactants in an attempt to prevent the metallic melt from diffusing through the ceramic containment used in the earlier core cell and interacting with the graphite heating element. Whenever this happens during a growth experiment the heater current invariably destabilizes and the experiment has to be arrested due to loss of temperature control. The second modification made in this reactor cell is that the metal melt is no longer pure gallium metal, as in the first, but is an alloy of 70% gallium and 30% manganese which was used in an attempt to increase the solubility of nitrogen in the melt and thus further promulgate growth of large GaN crystals. This alloy melt also has a higher melting point than pure gallium and as such is easier to handle without fear of contamination during core cell assembly and fabrication processes.

This reactor cell was loaded into the isopress and pressurized to a pressure of 1000atm, then the power was ramped by the same computer-programmed control program up to a heating element power throughput of 950W, which corresponds to an operating temperature of ~1150ºC ± 50ºC. The reactor core cell remained stable throughout the growth experiment, which lasted for 45 hours and was then arrested and recovered using the same process as the earlier experiments. Figure 3-36 shows SEM images taken from the resulting GaN crystals grown under high pressure in the isopress using the steel encapsulation and alloy melt in the reactor core cell. This GaN crystal was roughly the same size as in the earlier experiment, even though the process temperature was much lower.

XRD characterization was carried out on a selected crystal from this experiment using the same equipment as in the previous growth experiment, and the spectrum taken

is shown in Figure 3-37. This spectrum shows the same wurtzite-phase GaN (0002) and
(0004) peaks as the earlier sample, but also has a third peak at ~69° which we can
attribute to the (11-22) reflection of GaN, suggesting that a second GaN crystal was
present in the diffractometer, monolithically attached to the first, which produced the
(0002) reflection. There are also two smaller reflections visible (barely) in the spectrum,
which can be attributed to Mn_3N_2 when one takes into consideration the EDS spectrum
shown in Figure 3-38, which unsurprisingly shows clear presence of Mn in the spectrum
along with the Ga and N peaks. Acquisition of an XRD φ-scan, shown in Figure 3-39,
showed the (1 0 -1 0) planes spaced at regular 60° increments, just as in the previous
growth experiment, once again verifying the hexagonal GaN structure. The micro-
Raman spectrum shown in Figure 3-40, like that of the previously discussed experiment,
shows the characteristic transverse optic and longitudinal optic modes of wurtzite GaN,
again marked A1(TO), A1(LO), and E2 at Raman shifts of 528, 730 and 565 cm^{-1},
respectively.

The observed crystal growth in this work proceeded from spontaneously formed
nuclei in the Ga melt. Atomic nitrogen was provided in the melt through the thermal
dissolution/decomposition of the GaN source pellet at the operating pressure of the
system, via the following process:

$$GaN_{(s)} = Ga_{(melt)} + N_{(melt)} \tag{3-2}$$

where $Ga_{(melt)}$ and $N_{(melt)}$ indicate gallium and nitrogen dissolved in the melt region. The
reaction cell was designed to maintain a temperature gradient across the Ga melt region
adjacent to the source pellet, keeping the GaN source in the highest temperature zone,
thus allowing the dissolved nitrogen to diffuse to the lower temperature (lower solubility)
region of the melt where it then reacted to form new GaN. The crystal growth rate is

controlled by the flux of the dissolved nitrogen in the Ga melt in accordance with the expression:

$$J_N \propto \frac{\partial(c_N(x,T))}{\partial x},$$
(3-3)

where J_N is the flux of dissolved nitrogen, and the right-hand term is the temperature dependent concentration gradient of the dissolved nitrogen. Nitrogen readily exceeded the supersaturation concentration necessary for spontaneous, homogeneous nucleation in these experiments. This is due to the very low solubility of nitrogen in Ga metal, which is only ~0.1% at a temperature of 1600 K and 32 kbar pressure [87]. Increasing the pressure and the temperature of the Ga melt results in increased nitrogen solubility for faster growth due to the increased flux. Under the experimental conditions used, we expect the otherwise thermodynamically favored reaction:

$$N_{(melt)} + N_{(melt)} = N_{2\,(g)}$$
(3-4)

to be suppressed inside the reaction zone because of the large activation barrier associated with the high applied mechanical pressure and lack of free volume. We further expect that in the work involving the alloy melt, the solubility of nitrogen in the melt will be increased above that of pure gallium metal since the addition of Mn to the melt also increases the overall solubility in the melt, as nitrogen dissolves more readily in Mn than in Ga (the solubility of N in Mn at 1300C is 10 at. % in 1 atm of N_2 gas) and the overall solubility of the alloy melt is then a linear admixture of the solubilities of the components, weighted by their individual concentrations in the melt as in the expression:

$$S(Ga0.7Mn0.3) = 0.7*S(Ga) + 0.3*S(Mn)$$
(3-5)

as we've shown, but Mn alloying can also lead to the formation of unwanted phases upon cooling. Fortunately the crystals recovered showed good GaN growth despite this.
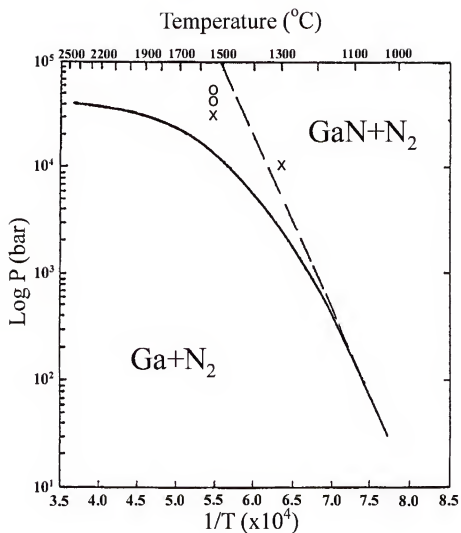
Figure 3-1. Results of the isopress GaN stability study superimposed on the GaN-N phase diagram.
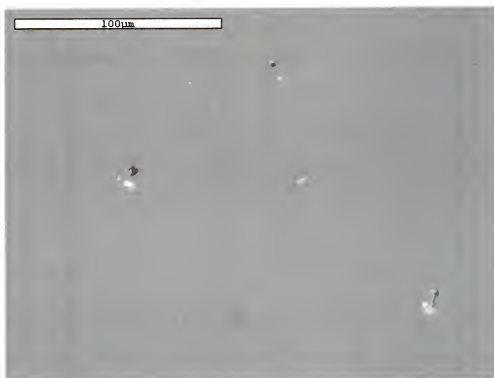
Figure 3-2. The SEM secondary electron image of as-received GaN film on sapphire substrate.
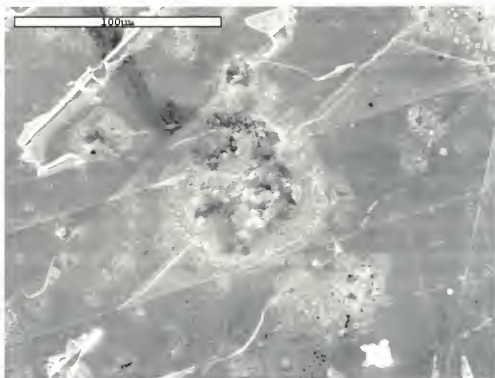
Figure 3-3. The SEM secondary electron image taken from the sample annealed under high pressure at 1100ºC.
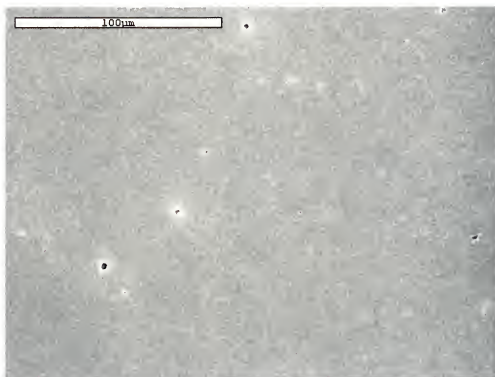
Figure 3-4. The SEM secondary electron image taken from the sample annealed at 1100°C under flowing argon gas.
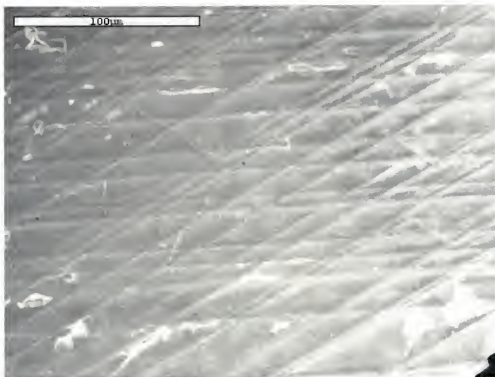
Figure 3-5. The SEM secondary electron image taken from the sample annealed under high pressure at 900°C.
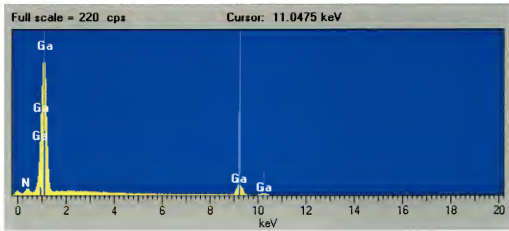
Figure 3-6. The EDS spectrum taken from as-received GaN film sample.
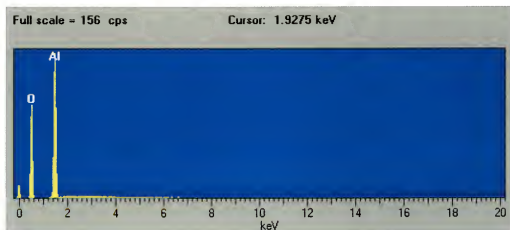
Figure 3-7. The EDS spectrum taken from the sample annealed at 1300ºC under flowing argon gas.

Figure 3-8. The EDS spectrum taken from the sample annealed under high pressure at 1300ºC.

A   B
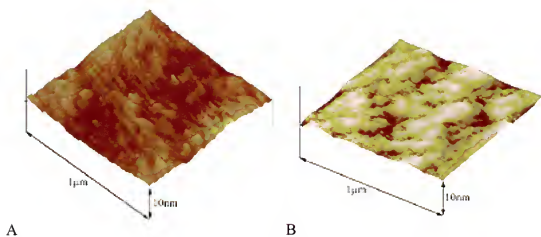
Figure 3-9. The AFM images taken from samples annealed at 900ºC A) under high-pressure and B) under flowing argon.
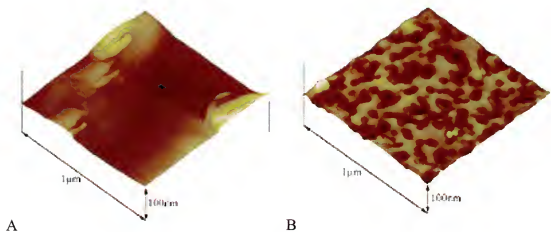
Figure 3-10. The AFM images taken from samples annealed at 1000ºC A) under high-pressure and B) under flowing argon.

A   B
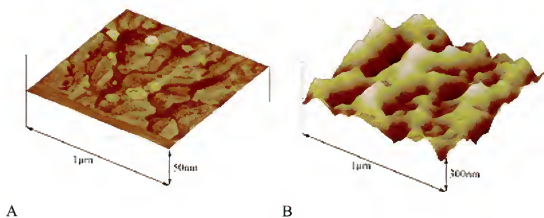
Figure 3-11. The AFM images taken from samples annealed at 1100ºC A) under high-pressure and B) under flowing argon.
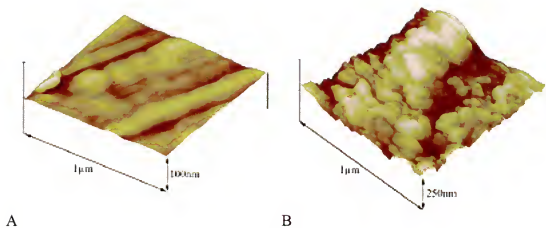
Figure 3-12. The AFM images taken from samples annealed at 1200ºC A) under high-pressure and B) under flowing argon.
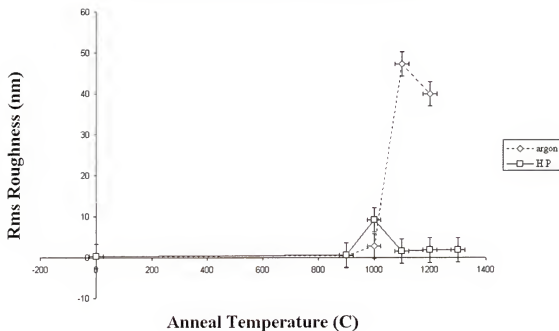
Figure 3-13. Comparison of the Rms roughness values obtained for samples annealed under high pressure (solid line) and those obtained for annealed performed under flowing argon (dashed line).
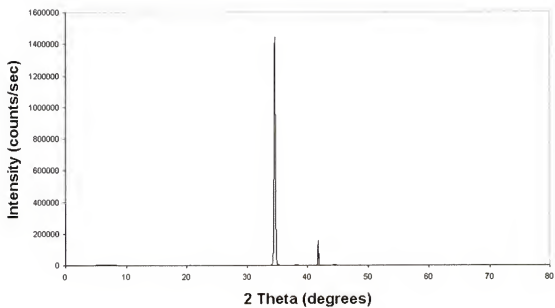
Figure 3-14. The XRD spectrum of an untreated sample of the same GaN film on sapphire substrate used in the annealing experiments.
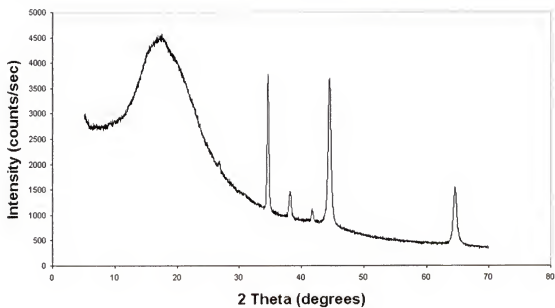
Figure 3-15. The XRD spectrum taken from the sample annealed at 1300°C under high pressure.
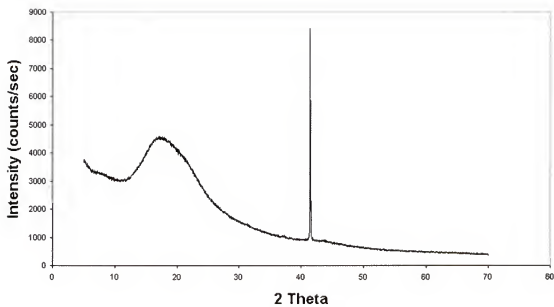
Figure 3-16. The XRD spectrum taken from the sample annealed under flowing argon gas at 1300ºC.
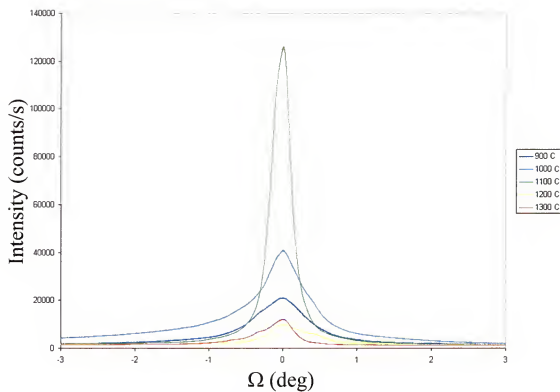
Figure 3-17. The Ω-scan rocking curves for the high-pressure samples superimposed on a single set of axes.
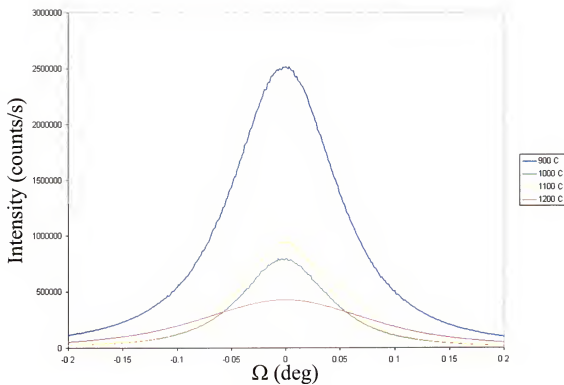
Figure 3-18. The Ω-scan rocking curves for the samples annealed in flowing argon gas superimposed on a single set of axes.
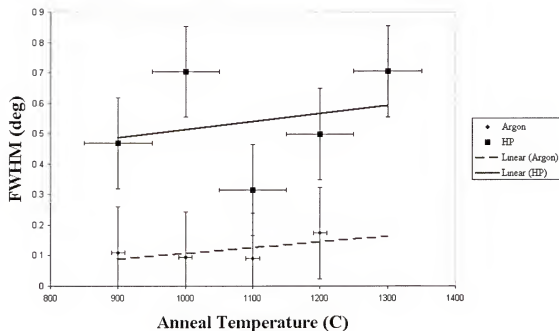
Figure 3-19. Comparison of the full width at half maximum (FWHM) values for the high-pressure and argon annealed sample Ω-scan rocking curves as a function of anneal temperature, with linear fits to the data computed by Microsoft Excel.

High Resolution XRD Curves for High Pressure Annealed Samples
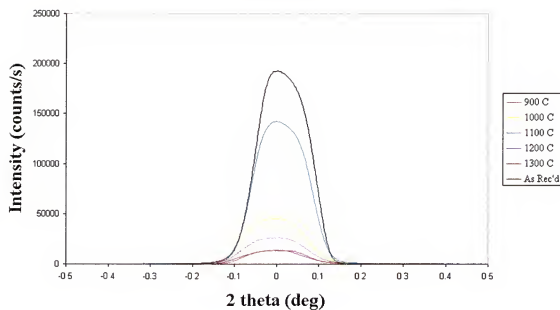
Figure 3-20. The $\Omega/2\theta$-scan rocking curves for the high-pressure samples superimposed on a single set of axes.

High Resolution XRD Curves for Ar Annealed Samples
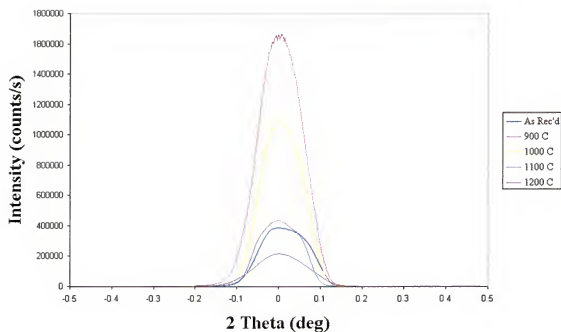
Figure 3-21. The $\Omega/2\theta$-scan rocking curves for the samples annealed in flowing argon gas superimposed on a single set of axes.
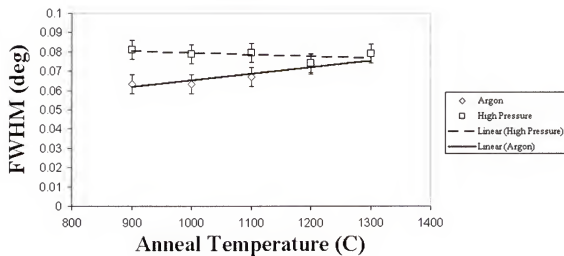
Figure 3-22. Comparison of the full width at half maximum (FWHM) values for the high-pressure and argon annealed sample $\Omega/2\theta$-scan rocking curves as a function of anneal temperature, with linear fits to the data computed by Microsoft Excel.
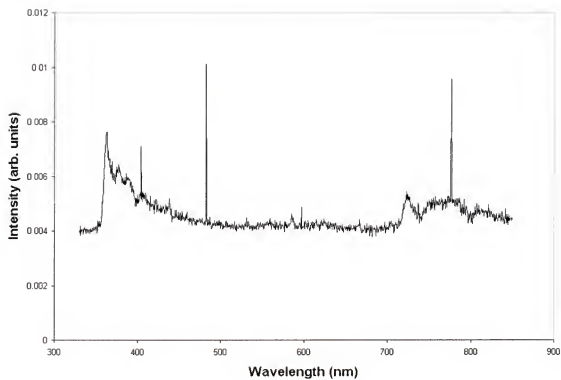
Figure 3-23. The PL spectrum taken from an untreated sample at 300K.
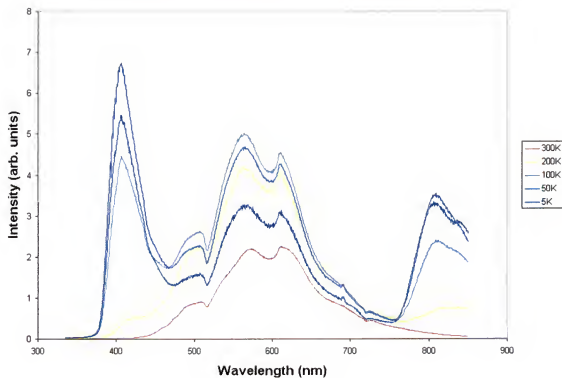
Figure 3-24. Sample annealed at 1100ºC under high pressure: PL spectra taken at 5, 50, 100, 200, and 300K.
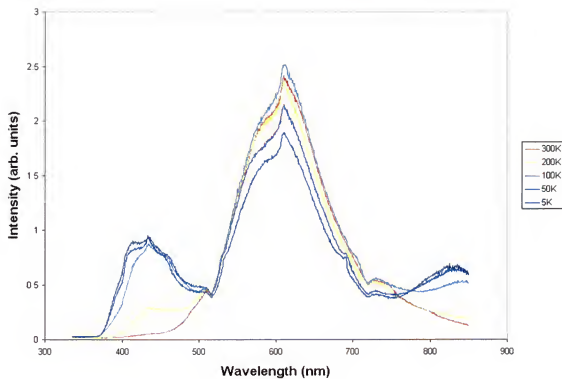
Figure 3-25. Sample annealed at 1200ºC under high pressure: PL spectra taken at 5, 50, 100, 200, and 300K.
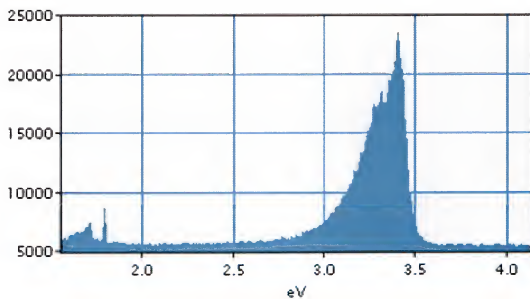
Figure 3-26. The CL spectrum taken from an as-received sample showing a prominent band-edge feature at around 3.4eV.
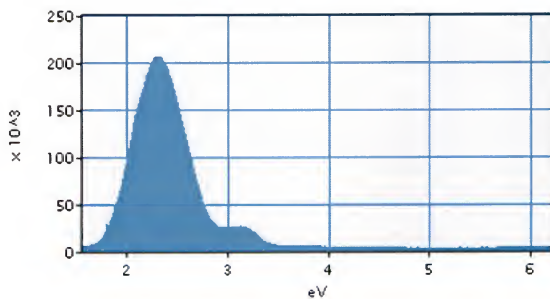
Figure 3-27. The CL spectrum taken from the sample annealed at 1100°C at high pressure showing a prominent yellow emission feature at around 2.25eV.

ZrO/CsCl   GaN

BN

Graphite   Ga
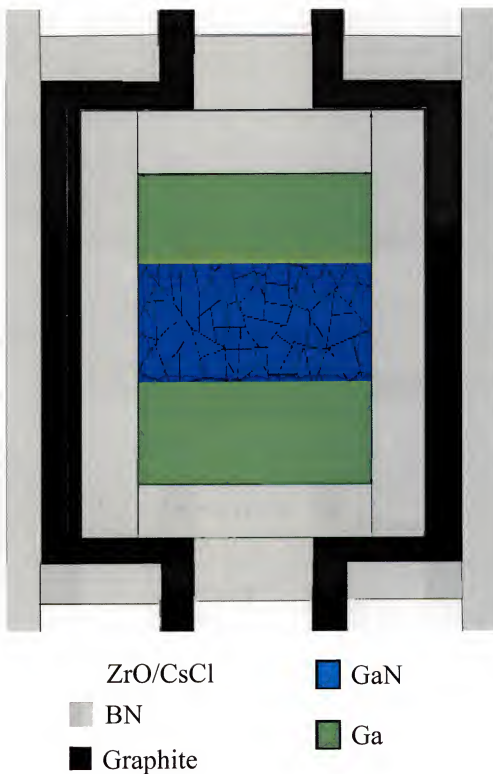
Figure 3-28: Isopress core cell geometry used for high pressure GaN crystal growth experiments.
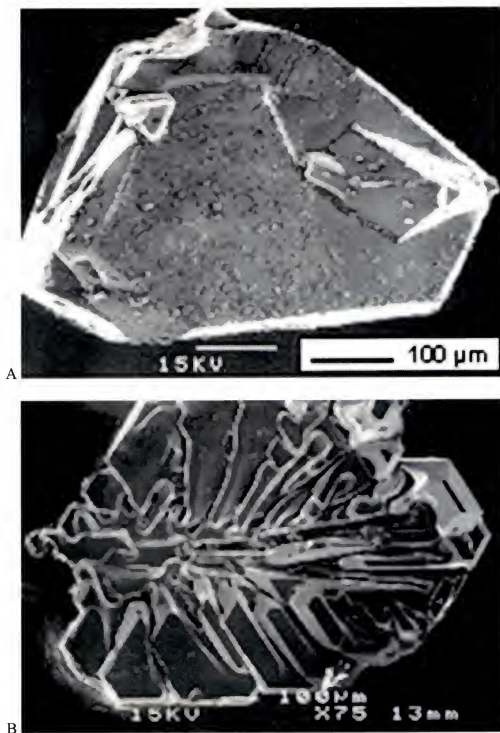
Figure 3-29. The SEM images of the crystals grown under high pressure in the isopress using pure gallium metal.
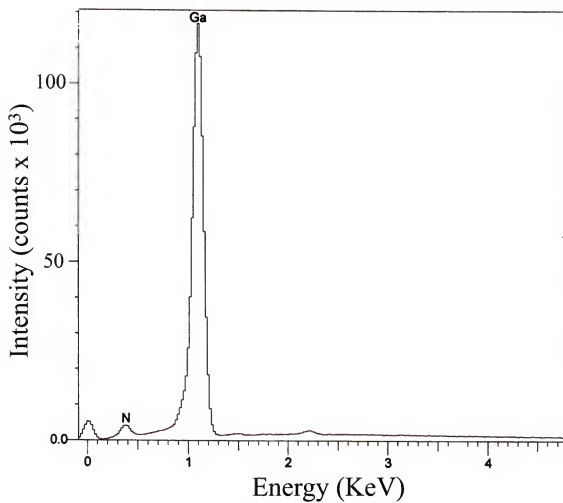
Figure 3-30. The EDS spectrum taken from the GaN crystals grown under high pressure using pure gallium metal.
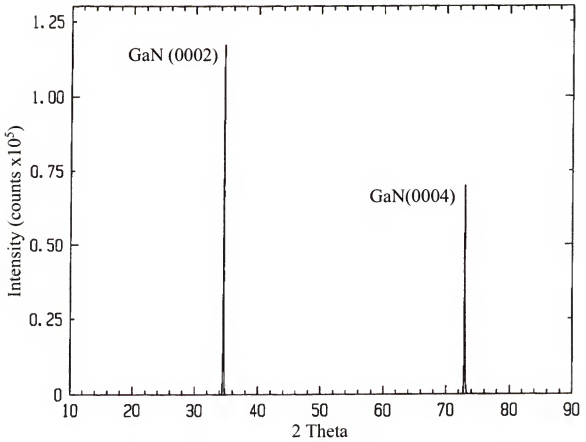
Figure 3-31. The XRD spectrum of a selected crystal grown under high pressure using pure gallium metal which shows prominent GaN (0002) and (0004) reflections.
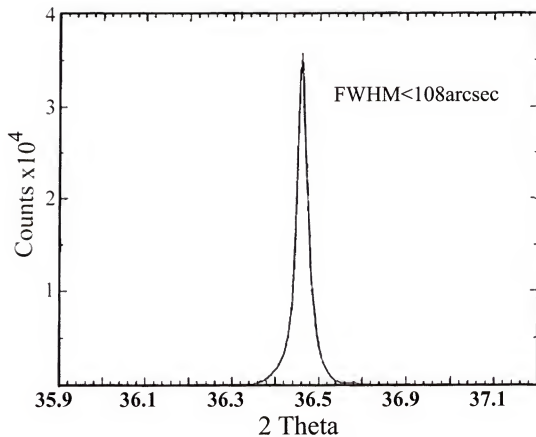
Figure 3-32. The XRD rocking curve of the GaN (0004) reflection taken from a selected crystal grown under high pressure using pure gallium.
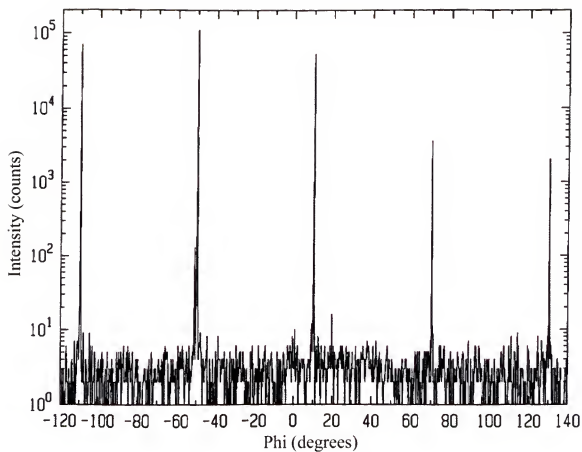
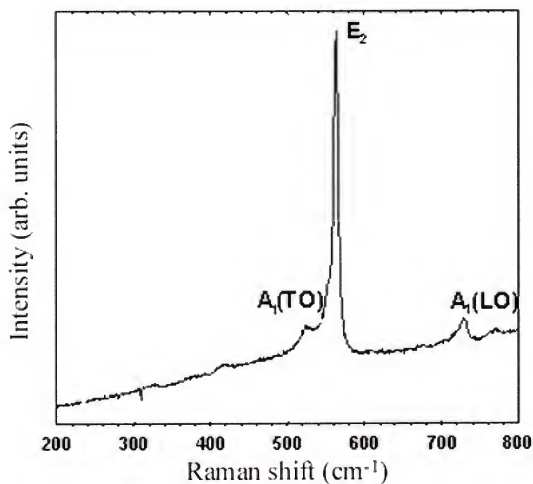Figure 3-33. The XRD φ-scan, plotted on a semi-logarithmic scale, showing a prominent set of GaN {10-10} reflections.

Figure 3-34. Micro-Raman spectrum taken from a selected crystal grown under high pressure using pure gallium metal.

▨ MgO		☐ ZrO/CsCl	
▨ Stainless Steel		▨ CsCl	
▨ 0.8CsCl/0.2BN		▨ GaN	
■ Graphite		■ 0.7Ga/0.3Mn	

Figure 3-35. Reactor core cell which used steel encapsulation and alloy melt.
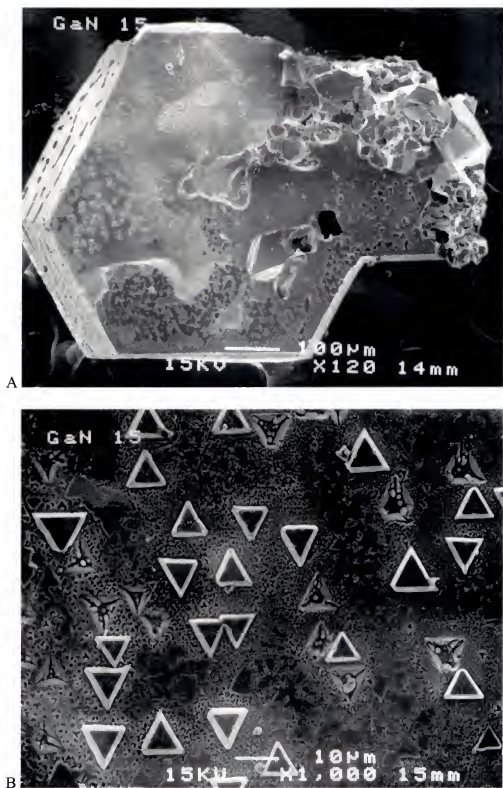
Figure 3-36. The SEM images of the crystals grown using steel encapsulation and an alloy melt.
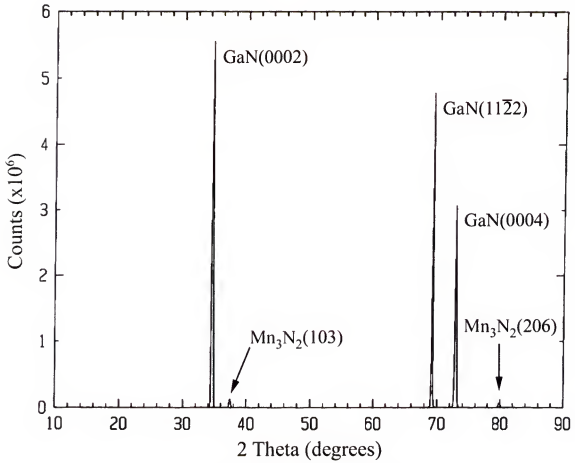
Figure 3-37. The XRD spectrum of the GaN crystals grown using steel encapsulation and an alloy melt.

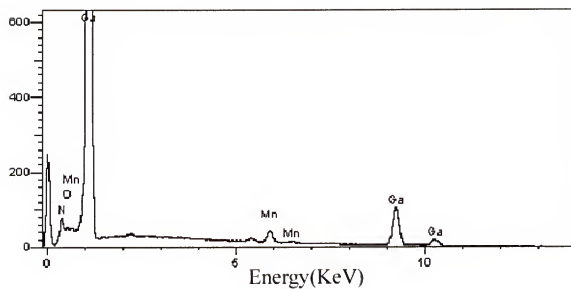Figure 3-38. The EDS spectrum taken from a crystal grown using steel encapsulation and an alloy melt, showing the presence of manganese and oxygen in small quantities.
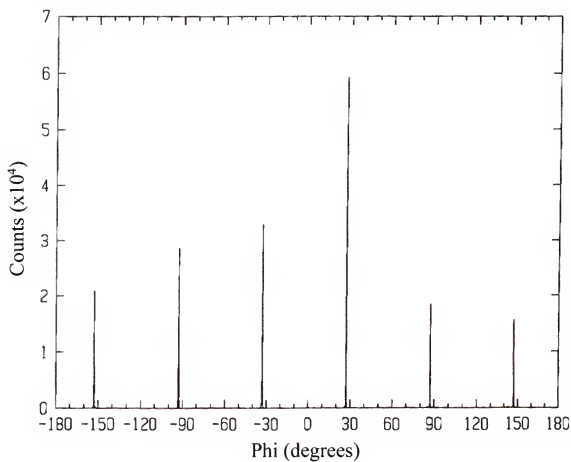
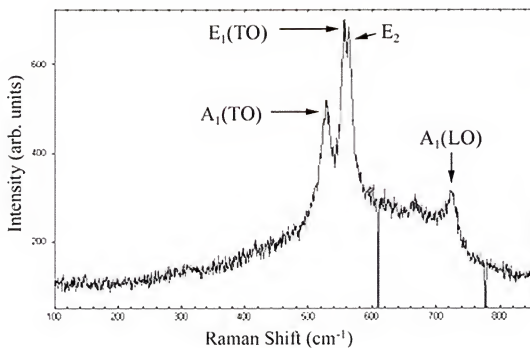Figure 3-39. The XRD φ-scan showing a prominent set of GaN {10-10} reflections at regular 60° intervals.

Figure 3-40. Micro-Raman spectrum taken from a selected crystal grown under high pressure using steel encapsulation and an alloy melt.

CHAPTER 4
CONCLUSIONS

A novel quasi-isostatic high-pressure system was employed to affect growth of GaN crystals from metallic melts containing dissolved GaN powder. This system was also employed to study the effects of annealing at high pressure on GaN thin film wafers grown on sapphire substrates via the MOCVD method.

High Pressure Annealing

While the tendency of GaN films to lose nitrogen at elevated temperatures has apparently been suppressed in the high-pressure system, judging by the AFM results, side effects of the high-pressure processing would appear to have crept into the annealing process. The films annealed under high pressure have prominent yellow emission in both the PL and CL spectra and their x-ray rocking curve FWHM values have broadened, most likely due to mechanical damage to the wafers in the case of the Ω-scans, and most likely due to increased carbon in the films in the case of the $\Omega/2\theta$-scans. The presence of spectral features in the PL spectra at 400 and 800nm respectively can be attributed to an exciton peak arising from the formation of nitrogen vacancies ion the films annealed and/or the p-type doping of the films as-received in the case of the peak at ~400nm, and most likely, second order diffraction of this exciton signal in the case of the peak at ~800nm.

In addition to this, the rocking curves and SEM images show that slip has occurred in the sapphire substrate along the (0001) direction in the prism planes. This is indicative of non-uniformities in the pressure applied by the isopress. The main causes for this are

twofold. Firstly, the isopress system is, to some extent, inherently non-isostatic. The pressure is applied with a hydraulic fluid to a pair of hemispherical gaskets and then transduced to the core via two sets of metal dies with gaskets between them. The pressure on the inner core is therefore applied somewhat triaxially, although at pressures exceeding ~30kbar the core volume can be considered a closed system with an ambient pressure determined by the triaxial pressure applied, scaled to the dimensions of the core.

The second reason for pressure non-uniformity is that the core cells, especially those used to anneal thin wafer samples, tend to deform somewhat upon pressure loading and application of heat. The amount of deformation is dependant on the shaping and construction of the cell itself, and is essentially a function of how well the various parts fit together. If two core parts are too loose or too tight, localized stresses will develop and can impact the pressure uniformity across the entire cell.

High Pressure Growth

The main goal of this work was to fabricate a monocrystalline volume of pure hexagonal GaN of several mm on a side. While this goal was not met, the crystals grown were of several hundred microns on a side and were measured to be of good crystalline quality and reasonable purity, as shown by the rocking curves, micro-Raman fingerprint analysis, and XRD spectra taken for selected crystals. The crystals were shown to be somewhat nitrogen deficient as shown by the EDS spectra. In the case of the crystals grown using the alloy melt, the presence of manganese in the system, which was added to increase the nitrogen solubility, seems to have led to the formation of a small amount of Mn_3N_2 which formed upon cooling, but did improve the solubility of nitrogen in the melft and allow us to obtain a small increase in growth speed.

The majority of the growth cells did not remain stable at the growth conditions attempted, and the main cause for this in most cases was not related to pressure non-uniformity, but to the tendency of gallium and/or manganese in the melt to leak or diffuse out of the inner core and interact with the cylindrical graphite heating element. Once the liquid metal diffuses into the graphite, the electrical properties of the heater change and can lead to rapid electrical failure of the system, which requires the system to be immediately shut down and the experiment therefore terminated well before the intended running time can be achieved. At best, melt-heater interactions simply cause immeasurable changes in the temperature distribution in the reactor cell volume, and at worst, the heater can fail altogether. A large part of this work was focused on trying to solve the problems of melt-heater interactions, and few achieved satisfactory results.

LIST OF REFERENCES

1. S. J. Pearton, F. Ren, A. P. Zhang, and K. P. Lee, Mat. Sci. Eng. **R30,** 55 (2000).

2. W. A. Melton, and J. I. Pankove, J. Crystal Growth **178,** 168 (1997).

3. K. Torii, S. F. Chichibu, T. Deguchi, H. Nakanishi, T. Sota, and S. Nakamura Physica B **302–303,** 268 (2001).

4. Y.Fu, H.Yang, D.G.Zhao, X.H.Zheng, S.F.Li, Y.P.Sun, Z.H.Feng, Y.T.Wang, and L.H.Duan, J. Crystal Growth **225,** 45 (2001).

5. C.C. Mitchell, M.E. Coltrin, and J. Han, J. Crystal Growth **222,** 144 (2001).

6. S. Porowski, Mat. Sci. & Eng. B **44** 407 (1997).

7. S. Porowski, J. Crystal Growth **166,** 583 (1996).

8. M. Leszczynski, I. Grzegory, H. Teisseyre, T. Suski, M. Bockowski, J. Jun, J.M. Baranowski, S. Porowski, and J. Domagala, J. Crystal Growth **169,** 235 (1996).

9. S. Porowski, and I. Grzegory, J. Crystal Growth **178,** 174 (1997).

10. I. Grzegory, and S. Porowski, Thin Solid Films **367,** 281 (2000).

11. T. Suski, P. Perlin, A. Pietraszko, M. Leszczynski, M. Bockowski, I. Grzegory, and S. Porowski, J. Crystal Growth **207,** 27 (1999).

12. T. Suski, J. Jun, M. Leszczynski, H. Teisseyre, I. Grzegory, S. Porowski, G. Dollinger, K. Saarinen, T. Laine, J. Nissila, W. Burkhard, W. Kriegseis, and B.K. Meyer, Mat. Sci. Eng. B **59** 1 (1999).

13. S. Porowski, J. Crystal Growth **189/190,** 153 (1998).

14. D. R. Ketchum, and J. W. Kolis J. Crystal Growth **222,** 431 (2001).

15. O. Kryliouk, M. Reed, T. Dann, T. Anderson, and B. Chai, Mat. Sci. Eng. B **66** 26 (1999).

16. M. K. Kelly, R. P. Vaudo, V. M. Phanse, L. Gorgens, O. Ambacher, and M. Stutzmann, J. Apl. Phys. **38** L217 (1999).

17. S.O. Kucheyev, J. S. Williams, and S. J. Pearton, Mat. Sci. Eng. **33**, 51 (2001).

18. J. A. Van Vechten, Phys. Rev. B **7**, 1479 (1973).

19. I. Grzegory, S. Krukowski, J. Jun, M. Bockowski, M. Wroblewski, B. Lucznik, and S. Porowski, J. Phys. Chem. Solids, **56**, 639 (1995).

20. I. Grzegory, and S. Porowski, J. Crystal Growth **66**, 11 (1984).

21. E. Alves, C. Liu, J. C. Waerenborgh, M. F. da Silva, and J. C. Soares, Nuc. Instr. Meth. Phys. Res. B **175**, 241 (2001).

22. M. Kappers, J. L. Guyaux, J. Olivier, R. Bisaro, C. Grattepain, and J.C. Garcia, Mat. Sci. Eng. B **59**, 52 (1999).

23. E. Alves, M.F. da Silva, J.C. Soares, R. Vianden, J. Bartels, and A. Kozanecki, Nuc. Instr. Meth. Phys. Res. B **147**, 383 (1999).

24. V.M. Bermudez, D.D. Koleske, and A.E. Wickenden, App. Surf. Sci. **126**, 69 (1998).

25. A. Pisch, and R. Schmid-Fetzer J. Crystal Growth **187**, 329 (1998).

26. O. Ambacher, M. S. Brandt, R. Dimitrov, T. Metzger, M. Stutzmann, R. A. Fischer, A. Miehr, A. Bergmaier , and G. Dollinger, J. Vac. Sci. Tech. B **14**, 3532 (1996).

27. R. G. Wilson, J. M. Zavada, X. A. Cao, R. K. Singh, S. J. Pearton, H. J. Guo, S. J. Pennycook, M. Fu, J. A. Sekhar, V. Scarvepalli, R. J. Shu, J. Han, D. J. Rieger, J. C. Zolper, and C. R. Abernathy, J. Vac. Sci. Tech. A **17**, 1226 (1999).

28. R. G. Wilson, S. J. Pearton, C. R. Abernathy, and J. M. Zavada, Appl. Phys. Lett. **66**, 2238 (1995).

29. C. Ronning, E. P. Carlson, D. B. Thomson, and R. F. Davis, Appl. Phys. Lett. **73**, 5 (1998).

30. C. Uzan-Saguy, J. Salzman, R. Kalish, V. Richter, U. Tish, S. Zamir, and S. Prawer, Appl. Phys. Lett. **74**, 2441 (1999).

31. D.C. Reynolds, D.C. Look, T. Wille, K.K. Bajaj, T.C. Collins, and R.J. Molnar, Sol. St. Comm. **109**, 683 (1999).

32. V. A. Joshkin ,C. A. Parker, S. M. Bedair, L. Y. Krasnobaev, J. J. Cuomo, R. F. Davis, and A. Suvkhanov, Appl. Phys. Lett. **72**, 2838 (1998).

33. B. Kaufmann, A. Dornen, V. Harle, H. Bolay, F. Scholz, and G. Pensl, Appl. Phys. Lett. **68**, 203 (1996).

34. T. Suski, J. Jun, M. Leszczynski, H. Teisseyre, S. Strite, A. Rockett, A. Pelzmann, M. Kamp, K. and J. Ebeling, J. Appl. Phys. **84**, 1155 (1998).

35. S. Fischer, G. Steude, D.M. Hofmann, F. Kurth, F. Anders, M. Topf, B.K. Meyer, F. Bertram, M. Schmidt, J. Christen, L. Eckey, J. Holst, A. Hofmann, B. Mensching, and B. Rauschenbach, J. Crystal Growth **190**, 556 (1998).

36. A. Wenzel, C. Liu, B. Rauschenbach Mat. Sci.Eng. B **59**, 191 (1999).

37. B. J. Pong, C. J. Pan, Y. C. Teng, G. C. Chi, W.-H. Li, and K. C. Lee, and C.-H Lee, J. Appl. Phys. **83**, 5992 (1998).

38. C. Ronning, M. Dalmer, M. Uhrmacher, M. Restle, U. Vetter, L. Ziegeler, H. Hofsass, T. Gehrke, K. Jarrendahl, and R. F. Davis, J. Appl. Phys. **87**, 2149 (2000).

39. S. O. Kucheyev, J. S. Williams, and C. Jagadish, J. Zou, and G. Li, J. Appl. Phys. **88**, 5493 (2000).

40. H. H. Tan, J. S. Williams, J. Zou, D. J. H. Cockayne, S. J. Pearton, J. C. Zolper, and R. A. Stall, Appl. Phys. Lett. **72**, 1190 (1998).

41. S. O. Kucheyev, J. S. Williams, C. Jagadish, G. Li, and S. J. Pearton, J. Appl. Phys. **76**, 3899(2000).

42. S. O. Kucheyev, J. S. Williams, J. Zou, C. Jagadish, and G. Li, Appl. Phys. Lett. **77**, 3577 (2000).

43. C. Liu, A. Wenzel, K. Volz, and B. Rauschenbach, Nuc. Inst. Meth. Phys. Res. B **148**, 396 (1999).

44. N. Parikh, A. Suvkhanov, M. Lioubtchenko, E. Carlson, M. Bremser, D. Bray, R. Davis, and J Hunn, Nuc. Inst. Meth. Phys. Res. B **127**, 463 (1997).

45. D. Byun, H. J. Kim, C. H. Hong, C. S. Park, G. Kim, S. K. Koh, W. K. Choi, and D.W. Kum, Phys. Stat. Sol. A **176**, 643 (1999).

46. O. Kryliouk, M. Reed, T. Dann, T. Anderson, and B. Chai, Mat. Sci. Eng. B **66**, 26 (1999).

47. C. T. Foxon, T. S. Cheng, S.V. Novikov, D. Korakakis, N. J. Jeffs, I. Grzegory, and S. Porowski, J. Crystal Growth **207**, 2 (1999).

48. R. J. Molnar, W. Gotz, L.T. Romano, and N. M. Johnson, J. Crystal Growth **178**, 147 (1997).

49. J. Karpinski, S. Porowski, and J. Jun, Mat. Res. Soc. Symp. Proc. **22**, 3 (1984).

50. J. M. Zavada, C. J. Ellis, J. Y. Lin, H. X. Jiang, J. T. Seo, U.Hommerich, M. Thaik, R. G. Wilson, P. A. Grudowski, and R.D. Dupuis, Mat. Sci. Eng. B **81**, 127 (2001).

51. E. Alves, T. Monteiro, J. Soares, L. Santos, M. F. da Silva, J. C. Soares, W. Lojkowski, D. Kolesnikov, R. Vianden, and J. G. Correia, Mat. Sci. Eng. B **81**, 132 (2001).

52. M. Overberg, K. N. Lee, C. R. Abernathy, S. J. Pearton, W.S. Hobson, R. G. Wilson, and J. M. Zavada, Mat. Sci. Eng. B **81**, 150 (2001).

53. S. J. Pearton, J. C. Zolper, R. J. Shul, and F. Ren, Appl. Phys. Rev. **86**, 3 (1999).

54. A. C. Schmitz, A. T. Ping, M. A. Khan, Q. Chen, J. W. Wang, and I. Adesida J. Elect.. Mat. **27**, 255 (1998).

55. H. P. Maruska and J. J. Tietjen, Appl. Phys. Lett. **15**, 327 (1969).

56. J. I. Pankove, E. A. Miller, and J. E. Berkeyheiser, RCA Rev. **32**, 383 (1971).

57. H. M. Manasevit, F. M. Erdmann, and W. I. Simpson, J. Electrochem. Soc. **118**, 1865 (1971).

58. I. Akasaki and I. Hayashi, Ind. Sci. Tech.. **17**, 48 (1976).

59. H. Amano, N. Sawaki, I. Akasaki, and Y. Toyoda, Appl. Phys. Lett. **48**, 353 (1986).

60. M. A. Khan, J. N. Kuznia, J. M. Van Hove, N. Pan, and J. Carter Appl. Phys. Lett. **60**, 3027 (1992).

61. J. Saito, k Nanbu, T. Ishikawa, and S. Hiyamizu, Jpn. J. Appl. Phys. **22**, L79 (1983).

62. M. A. Khan, T. N. Kuznia, A. R. Bhattaraia, and D. T. Olson, Appl. Phys. Lett. **62**, 1786 (1993).

63. M. A. Khan, A. R. Bhattaraia, J. N. Kuznia, and D. T. Olsen, Appl. Phys. Lett. **63**, 1214 (1993).

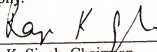64. S. Nakamura, T. Mukai, and M. Senoh, Appl. Phys. Lett. **64**, 1687 (1994).

65. S. C. Binari, L. B. Rowland, W. Kruppa, G. Kelner, K. Doverspike, and D. K. Gaskill, Elect. Lett. **30**, 1248 (1994).

66. M. A. Khan, J. N. Kuznia, D. T. Olsen, W. Schaff, J. Burm, and M. S. Shur, Appl. Phys. Lett. **65**, 1121 (1994).

67. J. Pankove, S. S. Chang, H. C. Lee, R. J. Molnar, T. D. Moustakas, and B. Van Zeghbroeck, IEEE IEDM, San Francisco, CA, 11–14 December 1994 (unpublished)., p.389

68. A. Ozgur, W. Kim, Z. Fan, A. Botchkarev, A. Salvador, S. N. Mohammad, B. Sverdlov, and H. Morkoc, Elect. Lett. **31**, 1389 (1995).

69. M. Dreschsler, D. M. Hofmann, B. K. Meyer, T. Detchprohm, H. Amano, and I. Akasaki, Jpn. J. Appl. Phys. **34**, L1178 (1995).

70. A. S. Barker, Jr. and M. Ilegems, Phys. Rev. B **7**, 743 (1973).

71. H. Sakai, T. Koide, H. Suzuki, M. Yamaguchi, S. Tamasaki, M. Koike, H. Amano, and I. Akasaki, Jpn. J. Appl. Phys Pt. 2 No. 11A **34**, L1430 (1995).

72. M. A. Khan, Q. Chen, M. S. Shur, B. T. Dermott, J. A. Higgins, J. Burm, W. Schaff, and L. F. Eastman, Elect.. Lett. **32**, 357 (1996).

73. J. C. Zolper, R. J. Shul, A. G. Baca, R. G. Wilson, S. J. Pearton, and R. A. Stall, Appl. Phys. Lett. **68**, 2273 (1996).

74. Y. F. Wu, B. P. Keller, S. Keller, D. Kapolnek, P. Kozodoy, S. P. Denbaars, and U. K. Mishra, Appl. Phys. Lett. **69**, 1438 (1996).

75. S. Nakamura and G. Fosol, *The Blue Laser Diode* (Springer, Berlin, 1998).

76. Y. F. Wu, B. P. Keller, P. Fim, J. Pusl, M. Le, N. X. Nguyen, C. Nguyen, D. Widman, S. Keller, S. P. Denbaars, and U. K. Mishra, Elect. Lett. **33**, 1743 (1997).

77. B. J. Thibeault, B. P. Keller, Y. F. Wu, P. Fina, U. K. Mishra, C. Nguyen, N. X. Nguyen, and M. Le, IEEE IEDM Washington, D.C., 7–10 December 1997 (unpunlished)., p569

78. G. J. Sullivan, M. Y. Chen, J. A. Higgins, J. W. Yang, Q. Chen, R. L. Pierson, and B. T. McDermott, IEEE Elect. Dev. Lett. **19**, 198 (1998).

79. L. S. McCarthy, P. Kozodoy, S. P. Denbaars, M. Rodwell, and U. K. Mishra, 25th Inter. Symp. On Comp. Semicond., 12–16 October 1998 (unpublished)., Nara, Japan, paper We2A-1

80. F. Ren, C. R. Abernathy, J. Van Hove, P. P. Chow, R. Hickman, K. B. Jung, H. Cho, T. LaRoche, R. J. Shul, J. Han, and S. J. Pearton, MRS Internet J. Nit. Semicond. Res. **3**, 41 (1998).

81. V. W. L. Chin, T. L. Tansley, and T. Osotchan, J. Appl. Phys. **81**, 7356 (1997).

82. S. N. Mohammad and H. Morkoc, Prog. Quant. Elect. **20**, 361 (1996).

83. M. S. Shur and M. A. Khan, Mat. Res. Bull. **22**, 44 (1997).

84. U. V. Bhapkar and M. S. Shur, J. Appl. Phys. **82**, 1649 (1997).

85. H.S. Kim and S. Roberts, J. Am. Ceram. Soc. **77**, 3099 (1994).

86. K. Peter, D. Lagerlof, A. H. Heuer, J. Castaing, J. P. Riviere, and T. E. Mitchell, J. Am. Ceram. Soc. **77**, 385 (1994).

87. S. Porowski and I. Grzegory, J. Elect. Eng. **3**, 80 (1994).

88. G. J. W. Kor, Mettal. Trans. B **9**, 97 (1978)

BIOGRAPHICAL SKETCH

Francis Kelly was born May 25, 1973 to Dr. and Mrs. Edward J. Kelly of Clarks Green, Pennsylvania. Francis took the middle name "Patrick" upon his confirmation at St. Gregory's Catholic Church in Clarks Summit, Pennsylvania. The youngest of four children, Francis attended Scranton Preparatory School in Scranton, Pennsylvania from 1988 to 1992 and upon his graduation he matriculated at Lehigh University in September of 1992 where he began his study of the physical sciences in earnest. He received his Bachelor of Arts degree in Physics at Lehigh in 1996 and, after receiving acceptance letters from both the University of Pittsburgh and the University of California at Davis, decided to remain at Lehigh and received his Masters of Science degree in Physics in 1998. The main branch of scientific research that Francis was involved in at Lehigh was the investigation of the effects of metal-hydrogen complexes in silicon under the direction of Dr. Michael Stovlola. Francis then matriculated at the University of Florida where he decided to dedicate himself to Materials Science and began his work on gallium nitride and high-pressure semiconductor processing techniques. He received his Masters in Materials Science and Engineering from the University of Florida in 2000, where his work in the high pressure processing of wide bandgap semiconductors continues.

I certify that I have read this study and that in my opinion it conforms to acceptable standards of scholarly presentation and is fully adequate, in scope and quality, as a dissertation for the degree of Doctor of Philosophy.
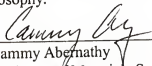
Rajiv K. Singh, Chairman
Professor of Materials Science and
Engineering

I certify that I have read this study and that in my opinion it conforms to acceptable standards of scholarly presentation and is fully adequate, in scope and quality, as a dissertation for the degree of Doctor of Philosophy.

Stephen J. Pearton
Professor of Materials Science and
Engineering

I certify that I have read this study and that in my opinion it conforms to acceptable standards of scholarly presentation and is fully adequate, in scope and quality, as a dissertation for the degree of Doctor of Philosophy.
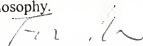
Cammy Abernathy
Professor of Materials Science and
Engineering

I certify that I have read this study and that in my opinion it conforms to acceptable standards of scholarly presentation and is fully adequate, in scope and quality, as a dissertation for the degree of Doctor of Philosophy.

Reza Abbaschian,
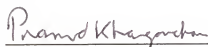Professor of Materials Science and
Engineering

I certify that I have read this study and that in my opinion it conforms to acceptable standards of scholarly presentation and is fully adequate, in scope and quality, as a dissertation for the degree of Doctor of Philosophy.

Fan Ren
Professor of Chemical Engineering

This dissertation was submitted to the Graduate Faculty of the College of Engineering and to the Graduate School and was accepted as partial fulfillment of the requirements for the degree of Doctor of Philosophy.

May 2003

Pramod P. Khargonekar
Dean, College of Engineering

Winfred M. Phillips
Dean, Graduate School